Glucose-stimulated KIF5B-driven microtubule sliding organizes microtubule networks in pancreatic beta cells

Kai M. Bracey[1], Pi'illani Noguchi[1], Courtney Edwards[2], Alisa Cario[1], Guoqiang Gu[1,3,4], Irina Kaverina[1,3]

Affiliations:

[1]Department of Cell and Developmental Biology, Vanderbilt University, Nashville, TN 37235, USA

[2]Department of Medicine, Vanderbilt University Medical Center, Nashville, TN 37232, USA.

[3]Program of Developmental Biology, Vanderbilt University, Nashville, TN 37232, USA.

[4]Center for Stem Cell Biology, Vanderbilt University, Nashville, TN 37232, USA.

Corresponding author: Irina Kaverina

Abstract

In pancreatic islet beta cells, molecular motors use cytoskeletal polymers microtubules as tracks for intracellular transport of insulin secretory granules. Beta-cell microtubule network has a complex architecture and is non-directional, which provide insulin granules at the cell periphery for rapid secretion response, yet to avoid over-secretion and subsequent hypoglycemia. We have previously characterized a peripheral sub-membrane microtubule array, which is critical for withdrawal of excessive insulin granules from the secretion sites. Microtubules in beta cells originate at the Golgi in the cell interior, and how the peripheral array is formed is unknown. Using real-time imaging and photo-kinetics approaches in clonal mouse pancreatic beta cells MIN6, we now demonstrate that kinesin KIF5B, a motor protein with a capacity to transport microtubules as cargos, slides existing microtubules to the cell periphery and aligns them to each other along the plasma membrane. Moreover, like many physiological beta-cell features, microtubule sliding is facilitated by a high glucose stimulus. These new data, together with our previous report that in high glucose sub-membrane MT array is destabilized to allow for robust secretion, indicate that MT sliding is another integral part of glucose-triggered microtubule remodeling, likely replacing destabilized peripheral microtubules to prevent their loss over time and beta-cell malfunction.

Introduction

The precise level of glucose-stimulated insulin secretion (GSIS) from pancreatic beta cells is crucial for glucose homeostasis. On one hand, insufficient insulin secretion decreases glucose uptake by peripheral tissues, leading to diabetes. On the other hand, excessive secretion causes glucose depletion from the bloodstream and hypoglycemia. Not surprisingly, multiple levels of cellular regulation control the amount of insulin secretory granules (IGs) released on every stimulus. One level of this control is facilitated by microtubules (MTs), intracellular polymers which serve as tracks for intracellular transport of IGs and define how many IGs are positioned at the secretion sites (Desai & Mitchison, 1997; Heaslip et al., 2014; Varadi, Ainscow, Allan, & Rutter, 2002).

Microtubules have a dual role in regulating the availability of IGs for secretion. Microtubules are necessary for efficient IG generation at the trans Golgi network (TGN). They are also required for IG transportation throughout the cell (Trogden et al., 2019; Zhu et al., 2015), which includes non-directional, diffusion-like redistribution in the cytoplasm (Tabei et al., 2013; Zhu et al., 2015) and directional runs of secretion-competent granules toward periphery (Hoboth et al., 2015; Muller et al., 2021). At the same time, peripheral IGs undergo MT-dependent withdrawal from the secretion sites, which prevents IG docking and acute over-secretion upon a given stimulus (Hu et al., 2021; Zhu et al., 2015). Such multi-faceted involvement of MT transport in secretion regulation is made possible by a complex architecture of MT networks in beta cells. To this end, interior beta-cell MTs are twisted and interlocked (Varadi, Tsuboi, Johnson-Cadwell, Allan, & Rutter, 2003; Zhu et al., 2015), which makes them dramatically distinct from radially organized MT arrays well-studied in generic cultured cell models and explains the predominantly non-

directional nature of IG transport (Bogan, 2021; Bracey, Gu, & Kaverina, 2022). Importantly, withdrawal of IGs and secretion restriction is achieved by a prominent array of MTs underlying cell membrane (Bracey et al., 2020). Under basal conditions, IGs are robustly withdrawn from the secretion sites along submembrane MTs, which are stabilized by MT-associated proteins (MAPs), including a well-known neuronal MAP tau (Ho et al., 2020). Upon a glucose stimulus, tau is phosphorylated and submembrane MTs become more dynamic (Ho et al., 2020) and fragmented, possibly via a MT-severing activity (Muller et al., 2021). Destabilization and partial depolymerization of submembrane MTs leads to IG docking and allows for secretion (Ho et al., 2020; Hu et al., 2021), probably as a consequence of decreased IG withdrawal by MT-dependent transport. Thus, existing data provide at least initial understanding of the mechanisms whereby beta-cell MT architecture allows for fine-tuning of secretion levels.

However, it is yet unclear how the complex beta-cell MT network forms. As in several other eukaryotic cells, MTs in beta cells are nucleated at MT-organizing centers (MTOCs) in the cell interior, partially at the centrosome and to a large extent at the Golgi membranes (Trogden et al., 2019; Zhu et al., 2015). Conventionally, this should be followed by MT plus-end polymerization toward the cell periphery and result in a radial MT array with high MT density in the center rather than in the periphery. The beta cell lacks such well-characterized MT polarity (Bracey et al., 2022). Thus, it is puzzling that the actual resulting MT system is non-radial and consists of an interior mesh a peripheral array (Bracey et al., 2020; Heaslip et al., 2014). How the beta cell organizes its cytoskeletal network for efficient trafficking of granules, and what factors contribute to the maintenance of the sub-membrane array, are important questions.

One of the established ways to modify the MT network without changing the location of MTOCs is to relocate already polymerized MTs by active motor-dependent transport. This phenomenon is called “MT sliding” (Straube, Hause, Fink, & Steinberg, 2006). Several MT-dependent

molecular motors have been implicated in driving MT sliding (Lu & Gelfand, 2017). In some cases, a motor facilitates MT sliding by walking along a MT while its cargo-binding domain is stationary being attached to a relatively large structure, e.g. plasma membrane. This causes sliding of a MT which served as a track for the stationary motor. This mechanism has been described for dynein-dependent MT sliding (Grabham, Seale, Bennecib, Goldberg, & Vallee, 2007; He et al., 2005). MTs can also be efficiently slid by motors which have two functional motor assemblies, such as a tetrameric kinesin-5/Eg5 (Acar et al., 2013; Vukusic, Ponjavic, Buda, Risteski, & Tolic, 2021), or which carry a MT as a cargo while walking along another MT. For the latter mechanism, a motor needs a non-motor domain with a capacity to bind either a MT itself, or a MT-associated protein as an adapter (Cao et al., 2020; Kurasawa, Earnshaw, Mochizuki, Dohmae, & Todokoro, 2004; Vukusic et al., 2021).

Out of these MT-sliding factors, kinesin-1 is known to be critical for organizing unusual MT architecture in specialized cells. In oocytes, kinesin-1-dependent MT sliding empowers cytoplasmic streaming (Barlan, Lu, & Gelfand, 2013). In differentiating neurons, kinesin-1 moves organelles and MTs into emerging neurites, which is a defining step in developing branched MT networks and long-distance neuronal transport (Jolly et al., 2010; Lu, Fox, Lakonishok, Davidson, & Gelfand, 2013). With these data in mind, kinesin-1 presents itself as the most attractive candidate for organizing MTs in beta cells. This motor highly expressed in beta cells and is well known to act as a major driving force in IG transport (Varadi et al., 2003).

Here, we show that KIF5B, encoding one of the three subunits of kinesin 1, actively slides MTs in beta cells and that this phenomenon defines MT network morphology and supplies MTs for the submembrane array. Moreover, we find that MT sliding in beta cells is a glucose-dependent process and thus likely participates in metabolically driven cell reorganization during each secretion cycle.

RESULTS

Identification of KIF5B as MT-sliding motor in beta cells

To address the factors that shape the configuration of MT networks in beta cells, we tested for a potential involvement of motors-dependent MT sliding. Not surprisingly, analysis of existing RNA-sequencing data in functional mouse islet beta cells highlighted kinesin-1 KIF5B as the highest expressing beta-cell motor protein (Fig. 1A) (Sanavia et al., 2021). Since this kinesin has been reported to have MT sliding activity in many types of interphase cells, we tested its potential ability to slide MTs in beta cells.

Efficient depletion of KIF5B was achieved by utilizing two independent lentiviral-based shRNA against mouse KIF5B in mouse insulinoma cell line MIN6 (Fig. 1B, Fig. 1- Suppl. Fig. 1A). To visualize MT sliding, shRNA-treated MIN6 cells expressing mEmerald-tubulin were imaged by live-cell spinning disk confocal microscopy. We photobleached MTs in two large cell regions leaving a thin unbleached band ("fluorescent belt") and analyzed relocation of MTs from the "fluorescent belt" into the bleached areas over time. To minimize the effects of plausible MT polymerization and to reduce photobleaching, MTs were imaged for short time periods (5 mins). Strikingly, in control cells (treated with scrambled control shRNA) MTs were efficiently translocated from the "fluorescent belt" into the photobleached area, indicating that MT sliding events are prominent in this cell type (Fig. 1C,D,). In contrast, MIN6 cells expressing either KIF5B shRNA variants displayed a significant loss of MT sliding ability (Fig. 1C,E,F, Fig.1-Video 1), indicating that the loss of KIFB leads to the loss of MT sliding.

While the assay described above provides an easy visualization of MT sliding, it allows for visualization of only a subset of the MT network. To further corroborate the above findings, we

used a less photodamaging system to visualize MT sliding that does not involve photobleaching and allows for evaluation of displacements within the whole MT network. To this end we applied a microtubule probe of fiducial marks, K560Rigor^{E236A}-SunTag (Tanenbaum, Gilbert, Qi, Weissman, & Vale, 2014) in MIN6 cells (Fig 1G-H). This probe contains the human kinesin-1 motor domain (residues 1–560) with a rigor mutation in the motor domain (K560Rigor^{E236A}) and fused to 24 copies of a GCN4 peptide. The rigor mutation in the motor domain causes it to bind irreversibly to microtubules (Rice et al., 1999). When co-expressed with a pHalo-tagged anti-GCN4 single-chain antibody (ScFv-GCN4-HaloTag-GB1-NLS), K560Rigor^{E236A} can recruit up to 24 of the Halo ligands to a single position on a microtubule. The pHalo- tagged anti GCN4 construct also contains a nuclear localization signal (NLS) which lends itself to reduce background of the unbound dye. This enables visualization of MT sliding events via single molecule tracking of the fiducial marks along the MT lattice, allowing us to analyze MT sliding behavior within the whole network with high temporal and spatial resolution (Fig. 1G-K, Fig. 1-Suppl. Fig. 1B, Fig.1-Video 2).

Our data indicate that in cells treated with scrambled control shRNA, a subset of K560Rigor^{E236A}-SunTag fiducial marks underwent rapid directional movements, interpreted as MT sliding events (Fig 1G, K). In contrast, majority of fiducial marks in cells expressing KIF5B-sepcific shRNAs were stationary (Fig. 1 H, I, J), indicating the lack of MT sliding. Collectively, these results indicate that KIF5B is necessary for MT sliding in MIN6 cells.

KIF5B is required for beta-cell MT organization

Because MT sliding mediated by KIF5B is a prominent phenomenon in beta cells, we sought to test whether it has functional consequences for MT networks in these cells. Tubulin immunostaining revealed striking differences in MT organization between MIN6 cells treated

with scrambled control shRNA versus KIF5B-specific shRNAs. While control cells had convoluted non-radial MTs with a prominent sub-membrane array, typical for beta cells (Fig. 2A), KIF5B-depleted cells featured extra-dense MTs in the cell center and sparse reseeding MTs at the periphery (Fig. 2B, C). Significant reduction of tubulin staining intensity at the cell periphery (Fig. 2D) confirms the robustness of this phenotype. This indicated that loss of KIF5B leads to a strong defect in MT location to the cell periphery.

KIF5B is required for beta-cell sub-membrane MT array alignment

Given the known significance of the peripheral MT array, which normally consists of well-organized MTs parallel to the cell membrane (Bracey et al., 2020), we have further analyzed directionally of MTs remaining at the cell periphery after KIF5B depletion. Previously we published a custom image analysis algorithm (Bracey et al., 2020) allowing for detailed quantitative characterization of MTs directionality in relation to the nearest cell border (Fig. 2 Supplemental Fig. 1). Here, we applied the same computational analysis to MT imaging data in MIN6 cells with perturbed KIF5B level and/or function. After deconvolution for increased signal-to-noise ratio, single 2D slices of MT images were subjected to thresholding optimized for the peripheral MT array (Fig. 2 Supplemental Fig. 2) and the directionality of MTs was determined in respect to the cell border. Every pixel of the image was analyzed with inconclusive pixels disregarded. Subsequently, MT directionality was quantified as a function of the distance from the cell border and directionality of peripheral MTs within 1µm of the cell border quantified. Our results indicate that in cells treated with non-targeting control shRNA (Fig. 2 F), the distribution of MT angles in the cell periphery are vastly parallel and co-aligned with the cell boundary, as previously reported for islet beta cells (Bracey et al. 2019). In contrast, the loss of KIF5B via shRNA depletion resulted in a significant loss of parallel MTs at the periphery (Fig. 2 G, H). This

indicated that MT sliding by KIF5B acts to align MT at the cell periphery in addition to delivering MTs to this cell location.

Combined, our data demonstrate a dramatic effect of KIF5B perturbation on both the distribution of MTs to the cell periphery and their orientation along the cell boundary. These data suggest that KIF5B-driven MT sliding is a decisive mechanism of the sub-membrane MT array generation, likely via redistribution of centrally nucleated MTs and subsequent aligning them at the cell edge. Thus, MT sliding is likely a critical component in functional MT organization in beta cells.

Beta-cell kinesin-1 drives MT sliding through the C-terminal MT-binding domain

While membrane cargo transport by KIF5s requires association of the heavy chain with the kinesin light chains (KLCs) and/or other adaptors, transportation of MTs as cargos occurs due to direct binding of KIF5 to MTs through the ATP-independent MT binding domain in heavy chain tail (C-terminus) (Jolly et al., 2010; Seeger & Rice, 2010).

To specifically establish the role of MT sliding by KIF5B in beta cells, we sought to evaluate the effects of suppressing the binding of KIF5B tail to MTs. To this end we used a previously generated construct (Ravindran, Engelke, Verhey, & Tsai, 2017), which is a motor-less version of wild-type (WT) kinesin-1 motor KIF5B containing the cargo-binding and ATP independent MT binding domain and tagged with mCherry (mCh) at the amino terminus (Fig 3A). When overexpressed, this construct acts as a dominant-negative (DN) tool preventing association of the tail of endogenous KIF5B with MTs. This tool is referred to as $KIFDN^{wt}$ (KIF5B dominant negative wild-type) moving forward (Fig. 3A).

To confirm that KIF5B tail domain binds to MTs in MIN6 and acts a dominant negative we co-expressed $KIFDN^{wt}$ and mEmerald-tubulin. When subjected to the FRAP assay we detected a

complete loss of MT sliding events as compared to a control (Fig. 3B-D). To prevent tail engagement of the MT lattice through the ATP-independent binding domain we opted to make point mutations in the tail domain to change the residues 892-DRKRYQ to 892-DAAAYA, thus generating KIFDN^{MUT} (Fig. 3A). Photobleaching assay in cells co-expressing of the KIFDN^{MUT} with mEmerald-tubulin indicated that the MT sliding activity was not blocked in the presence of the mutated construct (Fig. 3B, E, Fig.3-Video 1), confirming that KIF5B tail domain binding to MTs is needed for MT sliding in beta cells.

The dominant negative constructs are also tagged with the FK506-rapamycin-binding protein (FKBP), as indicated in Fig. 3A. This allows to heterodimerize them with a motor domain fused with the FKBP-rapamycin binding (FRB) domain using A/C Heterodimerizer (rapalog) and reconstitute a functional motor (Inobe & Nukina, 2016). We restored kinesin-1 activity by connecting the motor-less KIF5B, KIFDN^{wt}, to kinesin-1 motor domain as a way to rescue the effects of DN approach of KIF5B tail overexpression. To this end, we co-expressed MIN6 cells with the tail domain, mEmerald-tubulin, and the KIF5C motor domain fused to FRB domain (Fig. 3A). Once the tail and motor domain were dimerized with rapalog, we saw that the once blocked MT sliding events of the KIFDN^{wt} tail alone were now reversed (Fig. 3B, F, Fig.3-Video 2). In contrast, under conditions of heterodimerization of KIFDN^{MUT} with the motor, MT sliding was greatly impaired (Fig. 3B, G, Fig.3-Video 2), indicating that the motor with mutated ATP-independent binding domain cannot use MTs as cargos. Interestingly, endogenous motor in this case was unable to efficiently transport MTs, suggesting that the endogenous motor pool engaged in MT sliding was significantly smaller than the overexpressed non-functional motor.

Overall, the results of the DN approach confirm that MT sliding in beta cells is driven by KIF5B through direct kinesin-1 tail binding to cargo MTs.

Effects of C-terminal MT-binding of kinesin-1 on beta-cell MT organization

Keeping in mind that KIF5B has additional major functions in addition to MT sliding, we sought to test the consequence of MT sliding more directly by turning to overexpression of the DN constructs. Thus, we took advantage of our heterodimerization approach to analyze MT patterns in cells with active kinesin-1 which is able or unable to slide MTs (see Fig.3F vs Fig.3G). We analyzed MIN6 cells that express either the KIFDN^{wt} or KIFDN^{mut} tail domains alone (Fig. 4 Supplemental Fig. 1) or co-expressing and heterodimerized with the motor domain (Fig. 4B,C). Cells were fixed and immunostained for tubulin to identify the MT network. As expected, overexpression of the KIFDN^{WT} tail construct alone acted as dominant negative toward MT distribution to the cell periphery, resulting in decreased peripheral tubulin intensity (Fig. 4 Supplemental Fig. 1A,C), while in cells expressing KIFDN^{MUT} MT patterns were comparable to control (Fig. 4 Supplemental Fig. 1B,C).

Interestingly, expression of heterodimerized kinesin motors led to impaired MT network configurations compared to NT control (Fig. 4). Specifically, blocking of MT sliding by overexpression KIFDN^{mut} heterodimerized with the motor, led to the decrease in peripheral tubulin intensity (Fig. 4C,D) and impaired MT aligning along the cell border (Fig. 4E,G). These data indicate that KIF5B-driven relocation of centrally nucleated MTs to beta cell periphery requires kinesin tail domain binding to “cargo” MTs. Strikingly, overexpression of functional heterodimerized motor, which was capable of MT sliding and populating of the cell periphery with MTs as detected by tubulin intensity readings (KIFDN^{wt} heterodimerized with the motor, Fig. 4B,D), also led to a deficient MT aligning at the periphery (Fig. 4E,H). This can be interpreted as a result of unregulated sliding in these experimental conditions, since excessive kinesin-1-dependent sliding can lead to MT bending (Straube et al., 2006). This suggests that proper organization of MTs within the sub-membrane array requires fine tuning of MT sliding activity.

Collectively, this indicates that regulated KIF5B activity is essential for redistributing MTs to the cell border and sustaining an aligned peripheral MT array.

Exaggerated MT sliding leads to defects in peripheral array alignment

Our data discussed above suggest that overexpression of functional kinesin-1 disrupts MT alignment at the cell periphery, inducing their bending and buckling (Fig. 4E, G). To test if this defect is a result of excessive MT sliding, we employed a small molecule, kinesore, which is known to dramatically promote MT sliding by kinesisn-1 (Randall et al., 2017). Kinesore targets kinesin cargo adaptor function, by impairing KLC from binding kinesin heavy chain. As a result, kinesin heavy chain will excessively engage MTs through the C-terminal, ATP independent MT binding domain, leading to exaggerated MT sliding and the loss of membrane cargo transport by kinesin-1 (Randall et al., 2017).To this end we pretreated MIN6 cells with 50µm kinesore and stained for MTs (Fig. 5). MT networks in MIN6 cells became over corrected and looped (Fig. 5B) as previously seen in other cell types (Randall et al., 2017). This exaggerated MT looping resulting in a slight decrease of peripheral MT intensity (Fig. 5C). Further analysis of the peripheral bundle indicated that MT alignment was strongly impaired upon kinesore-driven MT remodeling as compared with vehicle (DMSO) treatment (Fig. 5D-G). The loss of coaligned MTs and loss of tubulin density at the periphery indicate that MT sliding must be gated to prevent over corrected MT networks.

MT sliding in beta cells is activated by glucose stimulation

It has previously been reported that kinesin-1 switches activity level in the presence of glucose stimuli (Donelan et al., 2002). We predicted that as KIF5B activity modulates the MT sliding events would also change depending on the glucose concentration. To test this, we pre-

incubated MIN6 cells with media containing a low concentration of 2.8mM glucose (Fig. 6A). We applied the photobleaching assay at these conditions and detected little to no MT sliding events. When switching glucose to a high concentration of 20mM, MT sliding and remodeling events were significantly increased (Fig. 6B, Fig.6-Video 1). Quantification of the sliding events demonstrated that MIN6 displaced MTs via MT sliding significantly more efficient upon glucose stimulation (Fig. 6C). We then turned to single molecule tracking of MT lattice fiducial marks (K560Rigor^{E236A}-SunTag) to further investigate this observation. Consistent with the photobleaching assay, the fiducial marks were predominantly stationary in cells pre-incubated in 2.8mM glucose (Fig. 6D) but frequently underwent directed relocation events indicative of MT sliding in cells after stimulated with 20mM glucose (Fig. 6E, Fig.6-Video 2).

These data demonstrate that glucose-stimulated remodeling of the MT network involves regulated MT sliding. Given the importance of MT sliding for peripheral MT organization (Figs. 2, 4), this effect may be essential to restore peripheral MT array after glucose-dependent destabilization or regulate other aspects of MT-dependent tuning of GSIS.

Discussion

Since the first description of convoluted MT network in MIN6 cells by the Rutter group (Varadi et al., 2003), our views on regulation, function, and dynamics of pancreatic beta cell MT network have been gradually evolving (Bracey et al., 2022). However, the field is still far from the understanding of the mechanisms underlying the network architecture. Here, we show that MT sliding is a prominent phenomenon in beta cells, and that it is driven by kinesin KIF5B. This kinesin-1-dependent MT sliding is a critical mechanism needed to formation and a long-term maintenance of beta cell MT network, especially the peripheral MT arrays, and that glucose

stimulation facilitates MT sliding activity. Overall, our study establishes MT sliding as an essential regulator of beta cell architecture and function.

Our data indicate that MT sliding is activated on a short-term basis after stimulation. It is plausible to suggest that this is needed to replace MTs at the cell periphery that are destabilized in high glucose after MT-stabilizing protein tau is phosphorylated and detached from the sub-membrane MTs (Ho et al., 2020). However, the amount of MT polymer on every glucose stimulation changes only slightly, often undetectable (Muller et al., 2021; Zhu et al., 2015). In fact, we observe a prominent effect of peripheral MT loss only after a long-term kinesin depletion (three-four days). This is consistent with our observation that only a minor subset of MT is being moved at every stimulation. We assume that the loss of peripheral MT array in KIF5B-depleted cells in a manifestation of accumulated lack of sliding over an extended period.

We also found that increasing MT sliding will also not yield a properly configured MT array: kinesore-treated cells lack aligned peripheral MTs. This indicates that, similar to other part of beta cell physiology, the dose of MT sliding has to be precisely tuned to achieve physiologically relevant architecture. It was shown before that exaggerated kinesin-dependent MT sliding causes MT bundling and buckling into aberrant configuration (Straube et al., 2006). We predict that a fine-tuning regulatory pathway must exist to restrict the number of MT sliding events to the cell needs.

Interestingly, blocking kinesin results in a striking accumulation of MT in the cell center where they are normally nucleated at MTOCs, which include the centrosome and the Golgi, in differentiated beta cells the latter being the main MTOC. Thus, sliding MTs originate from the MTOC area. At the same time, FIB-SEM analysis did not detect many MTs associated with MTOCs in physiologically normal beta cells (Muller et al., 2021). This implicates that MTs are normally rapidly dissociated from MTOCs so that they become available for transport by sliding. It is worth mentioning that for long-distance transport by sliding, cargo MTs must be short,

otherwise MT buckling and not long-distance transport will occur (Straube et al., 2006). Interestingly, Mueller shorter MTs have been observed in high glucose conditions (Muller et al., 2021), when MT are nucleated more actively (Trogden et al., 2019) and transported more frequently (this paper). Possibly, nucleated MTs are detached from MTOCs before they achieve a length that would prevent their transport. There is a possibility suggested that MTs are being severed by katanin in high glucose (Muller et al., 2021), which would generate MT fragments that can serve as cargos more easily. It is also possible that sliding MT subpopulation has some additional specific features that make them preferred cargos, since it is becoming increasingly clearer in the field that there is immense heterogeneity among MTs. Post-translational modifications and MT associated proteins, which vastly alter stability and coordination of motor proteins (Hammond, Cai, & Verhey, 2008; McKenney, Huynh, Vale, & Sirajuddin, 2016; Monroy et al., 2018; Yu, Garnham, & Roll-Mecak, 2015), might also influence which MTs serve as cargos versus transportation tracks in beta cells.

On a final note, it is important to evaluate the phenomenon reported here in light of the dual role of KIF5B as IG transporter and MT transporter and the coordination of those two roles in IG transport and availability for secretion. Our results indicate that KIF5B is needed for the patterning of peripheral MTs which we have shown to restrict secretion (Bracey et al., 2020; Ho et al., 2020). At the same time, it is well established that KIF5B transports IGs (Varadi et al., 2002) and KIF5B loss of function impairs insulin secretion (Cui et al., 2011). After a prolonged KIF5B inactivation, a loss of peripheral readily-releasable IG should be expected due to two factors: because there is no MT bundle to prevent over-secretion and IG depletion, and because there is no new IGs being transported from the Golgi area. In contrast, physiological activation of kinesin by glucose (Donelan et al., 2002; Varadi et al., 2003) would both promote replenishment of IG through non-directional transport through the cytoplasm and restoration of peripheral MT array to prevent over-secretion on each stimulus.

In conclusion, here we add another very important cell type to the list of systems that employ KIF5-dependent MT sliding to build functional MT networks. This system is unique because in this case MT sliding is metabolically regulated and activated on a single-minute time scale by nutrition triggers.

Materials and Methods

1. Key reagents

Reagent type or resource	**Designation**	**Source or reference**	**Additional information**
Cell line	MIN6		RRID:CVCL_0431
Chemical compound, drug	Kinesore	Tocris, Cat#: 6664	Final concentration (50µm)
Chemical compound, drug	A/C Heterodimerizing Drug	Takara, Cat#: 635056	Final concentration (25µm)
Antibody	Anti-KIF5B antibody	Abcam, Cat#: Ab167429	(1:500 dilution)
Antibody	Anti-alpha-Tubulin antibody	Sigma-Aldrich, Cat#: T9026	(1:500 dilution)
Halo Dye-585, 647	HaloTag® Ligands	CS315105, GA1120	2ul/mL

2. Cell Lines

MIN6 cells between passage 40-60 were utilized (Ishihara et al., 1993; Miyazaki et al., 1990). Cells were maintained in 25 mM glucose Dulbecco's modified eagle medium (DMEM) (Life Technologies, Frederick, MD) supplemented with 10% fetal bovine serum (FBS), 0.001% β-mercaptoethanol, 0.1 mg/ml penicillin, and 0.1 mg/ml streptomycin in 5% CO_2 at 37 degrees C.

3. Reagents and antibodies

Primary antibodies for immunofluorescence were: mouse anti-β-tubulin (Sigma-Aldrich, 1:1000), rabbit anti-β-tubulin (Sigma-Aldrich, 1:1000) and rabbit anti-KIF5B (Abcam), Alexa488-, Alexa568-, and Alexa647-conjugated highly cross-absorbed secondary antibodies (Invitrogen). Coverslips were mounted in Vectashield Mounting Medium (Vector Labaratories). Cells were treated with indicated drugs for three hours unless otherwise indicated. Drugs used were: Kinesore (Tocris Bioscience).

4. shRNA sequence

The KIF5B-targeting shRNA [shRNA KIF5B] #1, [TL510740B, 5'-ACTCTACGGAACACTATTCAGTGGCTGGA] and [shRNA KIF5B] #2, [TL51074CB 5' – AGACCGTAAACGCTATCAGCAAGAAGTAG] are in the plasmid backbone pGFP-C-shLenti and were from Origene (Rockville, MD). The non-targeting shRNA control, was pGFP-C-shLenti also from Origene.

5. DNA Constructs

Plasmid Construct	Source	Catalog #
SCR-TGFP	Origene	Custom
KIF5B shRNA#1-TGFP	Origene	Custom
KIF5B shRNA#2-TGFP	Origene	Custom
Scr shRNA mEmerald-Tubulin	This paper	Custom
KIF5B shRNA#1-mEmerald-tubulin	This paper	Custom
KIF5B shRNA#2-mEmerald-tubulin	This paper	Custom
mEmerald-Tubulin-C-18	Addgene	#54292
pcDNA4TO-K560-E236A-24xGCN4	Addgene	#60909
ScFv-GCN4-HaloTag-GB1-NLS	Addgene	#106303
FKBP-mCherry-KIF5B(568-964)	Kristen Verhey	((Ravindran et al., 2017))
p205ME_RnKIF5C(1-559)-TagBFP-FRB	Kristen Verhey	((Ravindran et al., 2017))
FKBP-mCherry-KIF5B(568-964)-AAAYA (MUT)	This paper	

6. Cloning

The Scr shRNA mEmerald-Tubulin, KIF5B shRNA#1-mEmerald-tubulin, KIF5B shRNA#2-mEmerald-tubulin were all generated from their respective TGFP containing constructs. Using the NotI and PmeI sites the TGFP was swapped for mEmerald-Tubulin.

The FKBP-mCherry-KIF5B(568-964) construct (gift from Kristen Verhey, University of Michigan), has previously been previously described (Ravindran et al., 2017).

By using site directed mutagenesis, we made 8 point mutations in the tail domain to change residues RKRYQ to AAAYA in the ATP independent MT binding domain. The point mutations were sufficient to rescue MT sliding in the cell. As previously published, this disrupts the tail domain to bind to the acidic e hook of the MT tail. Point mutations were introduced using a site directed mutagenesis kit, In-Fusion® Snap Assembly (Takara).

7. Lentiviral Transduction and Transfection

Lentivirus production and infection followed standard methods (Huang et al., 2018). MIN6 were treated with a given shRNA expressing a mEmerald-tubulin/cytosolic tgfp marker for 96hrs prior to imaging to achieve KD efficiency. For non-viral vectors, MIN6 cells were transfected using Amaxa Nucleofection (Lonza).

8. Western blotting

Cell lysates from MIN6 cells were lysed using 1% CHAPs buffer on ice for 5 minutes. For KIF5B knockdown, cells were first sorted for GFP expression after 72 h. Protein lysate (20µg) was loaded onto an 8% SDS-PAGE gel under reducing conditions and transferred to nitrocellulose

membranes. Membranes were probed with antibodies against KIF5B, and α-tubulin. The membranes were then blocked with 5% nonfat dried milk (Sigma-Aldrich) for 1 h and incubated overnight with primary antibodies: rabbit anti- KIF5B (Abcam), and mouse anti-GAPDH (Santa Cruz). anti-rabbit HRP and anti-mouse HRP were used as secondary antibodies and imaged on an ChemiDoc (Bio-Rad).

9. Image Acquisition

Immunofluorescence microscopy of fixed samples

Fixed samples were imaged using a laser scanning confocal microscope Nikon A1r based on a TiE Motorized Inverted Microscope using a 100X lens, NA 1.49, run by NIS Elements C software. Cells were imaged in 0.05μm slices through the whole cell.

Live cell imaging

Cells were cultured on 4-chamber MatTek dishes coated with 10 μg/μl fibronectin and transduced 96hrs or transfected 48 h before experiment. For live-cell imaging of MT sliding, cells were transfected with Emerald-Tubulin and imaged using a Nikon TiE inverted microscope equipped with 488- and 568-nm lasers, a Yokogawa CSU-X1 spinning disk head, a PLAN APO VC 100x NA1.4 oil lens, intermediate magnification 1.5X, and CMOS camera (Photometrics Prime 95B), 405 Burker mini-scanner, all controlled by Nikon Elements software.

Photobleaching Assay

~1x10^6 MIN6 cells were transfected with 1μg of mEmerald-tubulin or transduced with lentiviral KIF5B shRNA with mEmerald-tubulin as a reporter and attached to glass dishes coated with fibronectin for up to 96hrs. On the SDC microscope, the ROI tool in NIKON elements was used

to place two ROI's ~5μm apart at either end of the cell. These regions were assigned to be photobleached with the equipped 405nm mini scanner laser leaving a fluorescent patch over the middle which we termed the "fluorescent belt". After the regions were photobleached cells were then acquired for 5mins, across 7 optical slices (0.4μm step size) in 10 second interval between frames.

Sun Tag Rigor Kinesin and Tracking of MT sliding

SunTag system for MT lattice fiducial marks was adapted from (Lu, Winding, Lakonishok, Wildonger, & Gelfand, 2016). ~1x10^6 MIN6 cells were co transfected with 1μg of the ScFv-GCN4-HaloTag-GB1-NLS, and 0.5μg of the pcDNA4TO-K560-E236A-24xGCN4 plasmid (K560Rigor^{E236A}-SunTag (Tanenbaum et al., 2014)). After 24hrs the cells were washed with 1x PBS and the media replaced with KRB containing 2.8mM glucose for 1 hour, following a second incubation with HALO dye of choice (Promega) for 30mins. Cells were imaged in 1 focal plane for 2 mins with 100ms exposure time and no delay in acquisition. The acquired image was processed through Imaris Microscopy Image Analysis Software (Oxford Instruments), where the fiducial marks were tracked.

Sun Tag Rigor Kinesin Tracking Analysis

We sought to normalize the behaviors by comparing the MT movements over 5 second intervals and calculated the displacement of a given fiducial mark. In total over 60,000 tracks were detected, and the segmented displacement of ~25,000 of those tracks were calculated. The 5s displacement was binned at 0.05um intervals and the % of distribution for each bin was calculated for each cell and summarized in histograms (Fig 1, Fig 6).

10. Image Processing, and Analysis

Image processing

Figure 1: MaxIP (D-F), Single focal plane (G-I)

Figure 2: Cells shown are projections of the bottom 1µm of the cell. The tubulin channel was separated processed as gray value and inverted. The KIF5B channel was pseudo colored cyan and adjusted equally across all conditions (A-C) Single focal plane images under the nucleus of the cell were selected for analysis (F-H)

Figure 3: MaxIP of the tubulin channel for each time point (C-G)

Figure 4: Cells shown are projections of the bottom 1µm of the cell. The tubulin channel was separated processed as gray value and inverted (A-C).

Single focal plane images under the nucleus of the cell were selected for analysis (F-H) (see supplement Figure 2-1)

Figure 5: Cells shown are projections of the bottom 1µm of the cell. The tubulin channel was separated processed as gray value and inverted (A-B). Single focal plane images under the nucleus of the cell were selected for analysis (D-E)

Figure 6: MaxIP of the tubulin channel for each time point (A-B) Single plane (D-E)

MATLAB Script: MT Directionality

Oversampled images were deconvolved using the Richardson and Lucy Deconvolution algorithm. Images were masked and threshold (IsoData) in ImageJ. The MT directionality script was applied in MATLAB. Only the outer 1μm of MTs were taken for binning and quantification purposes.

MATLAB Script: Msdanalyzer, Segmentation

The position of all tracked fiducial spots were exported from Imaris to excel. The MSDanalyzer was developed by Nadine Tarantino et al, and adapted by Kai Bracey, Pi'Illani Noguchi, and Alisa Cario (Vanderbilt University) to normalize the tracks in time. Tracks were segmented into displacements over 5s and binned as shown in the results.

11. Statistics and reproducibility

For all experiments, *n* per group is as indicated by the figure legend and the scatter dot plots indicate the mean of each group and error bars indicate the standard error of the mean. All graphs and statistical analyses were generated using Excel (Microsoft) and Prism software (Graphpad). Statistical significance for all *in vitro* and *in vivo* assays was analyzed using an unpaired t-test, one-way ANOVA with Sidak's multiple comparisons test, Kolmogorov-Smirnov test as indicated in the figure legends. For each analysis $p < 0.05$ was considered statistically significant, and *$p < 0.05$, **$p < 0.01$, ***$p < 0.001$, ****$p < 0.0001$.

Author contributions

KMB performed most of the experiments and a large part of data analysis and wrote the manuscript. PN and AC provided scripts for data analysis and analyzed data. CE performed Western Blotting experiments. GG provided conceptual insight and molecular cloning strategy. I.K. supervised the study, provided conceptual insight and wrote the manuscript.

Acknowledgements

This work was supported by National Institutes of Health (NIH) grants F31DK122650 T32 (to KMB), R35-GM127098 (to I.K.), R01-DK106228 (to I.K. and G.G.), R01-DK65949 (to G. G.), R01-DK125696 (to G.G.). KMB was supported by an NIH training grant R25-GM062459 “Initiative for Maximize Student Diversity” (Sealy, PI), AC by an NIH training grant T32-CA119925 “Integrated Biological Systems Training in Oncology” (Tansey, PI), CME was supported by NIGMS of the NIH under award number T32GM007347, and PN by an NIH training grant T32 DK101003 “Integrated Training in Engineering and Diabetes” (Young, PI). We thank Hamida Ahmed for technical help. The authors also thank Margret Fye for critical reading of the manuscript.

References

Acar, S., Carlson, D. B., Budamagunta, M. S., Yarov-Yarovoy, V., Correia, J. J., Ninonuevo, M. R., . . . Scholey, J. M. (2013). The bipolar assembly domain of the mitotic motor kinesin-5. *Nat Commun, 4*, 1343. Retrieved from https://www.ncbi.nlm.nih.gov/pubmed/23299893. doi:10.1038/ncomms2348

Barlan, K., Lu, W., & Gelfand, V. I. (2013). The microtubule-binding protein ensconsin is an essential cofactor of kinesin-1. *Curr Biol, 23*(4), 317-322. Retrieved from https://www.ncbi.nlm.nih.gov/pubmed/23394833. doi:10.1016/j.cub.2013.01.008

Bogan, J. S. (2021). Granular detail of beta cell structures for insulin secretion. *J Cell Biol, 220*(2). Retrieved from https://www.ncbi.nlm.nih.gov/pubmed/33427875. doi:10.1083/jcb.202012082

Bracey, K. M., Gu, G., & Kaverina, I. (2022). Microtubules in Pancreatic beta Cells: Convoluted Roadways Toward Precision. *Front Cell Dev Biol, 10*, 915206. Retrieved from https://www.ncbi.nlm.nih.gov/pubmed/35874834. doi:10.3389/fcell.2022.915206

Bracey, K. M., Ho, K. H., Yampolsky, D., Gu, G., Kaverina, I., & Holmes, W. R. (2020). Microtubules Regulate Localization and Availability of Insulin Granules in Pancreatic Beta Cells. *Biophys J, 118*(1), 193-206. Retrieved from https://www.ncbi.nlm.nih.gov/pubmed/31839261. doi:10.1016/j.bpj.2019.10.031

Cao, Y., Lipka, J., Stucchi, R., Burute, M., Pan, X., Portegies, S., . . . Hoogenraad, C. C. (2020). Microtubule Minus-End Binding Protein CAMSAP2 and Kinesin-14 Motor KIFC3 Control Dendritic Microtubule Organization. *Curr Biol, 30*(5), 899-908 e896. Retrieved from https://www.ncbi.nlm.nih.gov/pubmed/32084403. doi:10.1016/j.cub.2019.12.056

Cui, J., Wang, Z., Cheng, Q., Lin, R., Zhang, X. M., Leung, P. S., . . . Huang, J. D. (2011). Targeted inactivation of kinesin-1 in pancreatic beta-cells in vivo leads to insulin secretory deficiency. *Diabetes, 60*(1), 320-330. Retrieved from https://www.ncbi.nlm.nih.gov/pubmed/20870970. doi:10.2337/db09-1078

Desai, A., & Mitchison, T. J. (1997). Microtubule polymerization dynamics. *Annu Rev Cell Dev Biol, 13*, 83-117. Retrieved from https://www.ncbi.nlm.nih.gov/pubmed/9442869. doi:10.1146/annurev.cellbio.13.1.83

Donelan, M. J., Morfini, G., Julyan, R., Sommers, S., Hays, L., Kajio, H., . . . Rhodes, C. J. (2002). Ca2+-dependent dephosphorylation of kinesin heavy chain on beta-granules in pancreatic beta-cells. Implications for regulated beta-granule transport and insulin exocytosis. *J Biol Chem, 277*(27), 24232-24242. Retrieved from https://www.ncbi.nlm.nih.gov/pubmed/11978799. doi:10.1074/jbc.M203345200

Grabham, P. W., Seale, G. E., Bennecib, M., Goldberg, D. J., & Vallee, R. B. (2007). Cytoplasmic dynein and LIS1 are required for microtubule advance during growth cone remodeling and fast axonal outgrowth. *J Neurosci, 27*(21), 5823-5834. Retrieved from https://www.ncbi.nlm.nih.gov/pubmed/17522326. doi:10.1523/JNEUROSCI.1135-07.2007

Hammond, J. W., Cai, D., & Verhey, K. J. (2008). Tubulin modifications and their cellular functions. *Curr Opin Cell Biol, 20*(1), 71-76. Retrieved from https://www.ncbi.nlm.nih.gov/pubmed/18226514. doi:10.1016/j.ceb.2007.11.010

He, Y., Francis, F., Myers, K. A., Yu, W., Black, M. M., & Baas, P. W. (2005). Role of cytoplasmic dynein in the axonal transport of microtubules and neurofilaments. *J Cell Biol, 168*(5), 697-703. Retrieved from https://www.ncbi.nlm.nih.gov/pubmed/15728192. doi:10.1083/jcb.200407191

Heaslip, A. T., Nelson, S. R., Lombardo, A. T., Beck Previs, S., Armstrong, J., & Warshaw, D. M. (2014). Cytoskeletal dependence of insulin granule movement dynamics in INS-1 beta-cells in response to glucose. *PLoS One, 9*(10), e109082. Retrieved from https://www.ncbi.nlm.nih.gov/pubmed/25310693. doi:10.1371/journal.pone.0109082

Ho, K. H., Yang, X., Osipovich, A. B., Cabrera, O., Hayashi, M. L., Magnuson, M. A., . . . Kaverina, I. (2020). Glucose Regulates Microtubule Disassembly and the Dose of Insulin Secretion via Tau Phosphorylation. *Diabetes, 69*(9), 1936-1947. Retrieved from https://www.ncbi.nlm.nih.gov/pubmed/32540877. doi:10.2337/db19-1186

Hoboth, P., Muller, A., Ivanova, A., Mziaut, H., Dehghany, J., Sonmez, A., . . . Solimena, M. (2015). Aged insulin granules display reduced microtubule-dependent mobility and are disposed within actin-positive multigranular bodies. *Proc Natl Acad Sci U S A, 112*(7), E667-676. Retrieved from https://www.ncbi.nlm.nih.gov/pubmed/25646459. doi:10.1073/pnas.1409542112

Hu, R., Zhu, X., Yuan, M., Ho, K. H., Kaverina, I., & Gu, G. (2021). Microtubules and Galphao-signaling modulate the preferential secretion of young insulin secretory granules in islet beta cells via independent pathways. *PLoS One, 16*(7), e0241939. Retrieved from https://www.ncbi.nlm.nih.gov/pubmed/34292976. doi:10.1371/journal.pone.0241939

Huang, C., Walker, E. M., Dadi, P. K., Hu, R., Xu, Y., Zhang, W., . . . Gu, G. (2018). Synaptotagmin 4 Regulates Pancreatic beta Cell Maturation by Modulating the Ca(2+) Sensitivity of Insulin Secretion Vesicles. *Dev Cell, 45*(3), 347-361 e345. Retrieved from https://www.ncbi.nlm.nih.gov/pubmed/29656931. doi:10.1016/j.devcel.2018.03.013

Inobe, T., & Nukina, N. (2016). Rapamycin-induced oligomer formation system of FRB-FKBP fusion proteins. *J Biosci Bioeng, 122*(1), 40-46. Retrieved from https://www.ncbi.nlm.nih.gov/pubmed/26777239. doi:10.1016/j.jbiosc.2015.12.004

Ishihara, H., Asano, T., Tsukuda, K., Katagiri, H., Inukai, K., Anai, M., . . . Oka, Y. (1993). Pancreatic beta cell line MIN6 exhibits characteristics of glucose metabolism and glucose-stimulated insulin secretion similar to those of normal islets. *Diabetologia, 36*(11), 1139-1145. Retrieved from https://www.ncbi.nlm.nih.gov/pubmed/8270128. doi:10.1007/BF00401058

Jolly, A. L., Kim, H., Srinivasan, D., Lakonishok, M., Larson, A. G., & Gelfand, V. I. (2010). Kinesin-1 heavy chain mediates microtubule sliding to drive changes in cell shape. *Proc Natl Acad Sci U S A, 107*(27), 12151-12156. Retrieved from https://www.ncbi.nlm.nih.gov/pubmed/20566873. doi:10.1073/pnas.1004736107

Kurasawa, Y., Earnshaw, W. C., Mochizuki, Y., Dohmae, N., & Todokoro, K. (2004). Essential roles of KIF4 and its binding partner PRC1 in organized central spindle midzone formation. *EMBO J, 23*(16), 3237-3248. Retrieved from https://www.ncbi.nlm.nih.gov/pubmed/15297875. doi:10.1038/sj.emboj.7600347

Lu, W., Fox, P., Lakonishok, M., Davidson, M. W., & Gelfand, V. I. (2013). Initial neurite outgrowth in Drosophila neurons is driven by kinesin-powered microtubule sliding. *Curr*

561 *Biol, 23*(11), 1018-1023. Retrieved from
562 https://www.ncbi.nlm.nih.gov/pubmed/23707427. doi:10.1016/j.cub.2013.04.050
563 Lu, W., & Gelfand, V. I. (2017). Moonlighting Motors: Kinesin, Dynein, and Cell Polarity. *Trends*
564 *Cell Biol, 27*(7), 505-514. Retrieved from
565 https://www.ncbi.nlm.nih.gov/pubmed/28284467. doi:10.1016/j.tcb.2017.02.005
566 Lu, W., Winding, M., Lakonishok, M., Wildonger, J., & Gelfand, V. I. (2016). Microtubule-
567 microtubule sliding by kinesin-1 is essential for normal cytoplasmic streaming in
568 Drosophila oocytes. *Proc Natl Acad Sci U S A, 113*(34), E4995-5004. Retrieved from
569 https://www.ncbi.nlm.nih.gov/pubmed/27512034. doi:10.1073/pnas.1522424113
570 McKenney, R. J., Huynh, W., Vale, R. D., & Sirajuddin, M. (2016). Tyrosination of alpha-tubulin
571 controls the initiation of processive dynein-dynactin motility. *EMBO J, 35*(11), 1175-
572 1185. Retrieved from https://www.ncbi.nlm.nih.gov/pubmed/26968983.
573 doi:10.15252/embj.201593071
574 Miyazaki, J., Araki, K., Yamato, E., Ikegami, H., Asano, T., Shibasaki, Y., . . . Yamamura, K. (1990).
575 Establishment of a pancreatic beta cell line that retains glucose-inducible insulin
576 secretion: special reference to expression of glucose transporter isoforms.
577 *Endocrinology, 127*(1), 126-132. Retrieved from
578 https://www.ncbi.nlm.nih.gov/pubmed/2163307. doi:10.1210/endo-127-1-126
579 Monroy, B. Y., Sawyer, D. L., Ackermann, B. E., Borden, M. M., Tan, T. C., & Ori-McKenney, K. M.
580 (2018). Competition between microtubule-associated proteins directs motor transport.
581 *Nat Commun, 9*(1), 1487. Retrieved from
582 https://www.ncbi.nlm.nih.gov/pubmed/29662074. doi:10.1038/s41467-018-03909-2
583 Muller, A., Schmidt, D., Xu, C. S., Pang, S., D'Costa, J. V., Kretschmar, S., . . . Solimena, M. (2021).
584 3D FIB-SEM reconstruction of microtubule-organelle interaction in whole primary
585 mouse beta cells. *J Cell Biol, 220*(2). Retrieved from
586 https://www.ncbi.nlm.nih.gov/pubmed/33326005. doi:10.1083/jcb.202010039
587 Randall, T. S., Yip, Y. Y., Wallock-Richards, D. J., Pfisterer, K., Sanger, A., Ficek, W., . . . Dodding,
588 M. P. (2017). A small-molecule activator of kinesin-1 drives remodeling of the
589 microtubule network. *Proc Natl Acad Sci U S A, 114*(52), 13738-13743. Retrieved from
590 https://www.ncbi.nlm.nih.gov/pubmed/29229862. doi:10.1073/pnas.1715115115
591 Ravindran, M. S., Engelke, M. F., Verhey, K. J., & Tsai, B. (2017). Exploiting the kinesin-1
592 molecular motor to generate a virus membrane penetration site. *Nat Commun, 8*,
593 15496. Retrieved from https://www.ncbi.nlm.nih.gov/pubmed/28537258.
594 doi:10.1038/ncomms15496
595 Rice, S., Lin, A. W., Safer, D., Hart, C. L., Naber, N., Carragher, B. O., . . . Vale, R. D. (1999). A
596 structural change in the kinesin motor protein that drives motility. *Nature, 402*(6763),
597 778-784. Retrieved from https://www.ncbi.nlm.nih.gov/pubmed/10617199.
598 doi:10.1038/45483
599 Sanavia, T., Huang, C., Manduchi, E., Xu, Y., Dadi, P. K., Potter, L. A., . . . Gu, G. (2021). Temporal
600 Transcriptome Analysis Reveals Dynamic Gene Expression Patterns Driving beta-Cell
601 Maturation. *Front Cell Dev Biol, 9*, 648791. Retrieved from
602 https://www.ncbi.nlm.nih.gov/pubmed/34017831. doi:10.3389/fcell.2021.648791

603 Seeger, M. A., & Rice, S. E. (2010). Microtubule-associated protein-like binding of the kinesin-1
604 tail to microtubules. *J Biol Chem, 285*(11), 8155-8162. Retrieved from
605 https://www.ncbi.nlm.nih.gov/pubmed/20071331. doi:10.1074/jbc.M109.068247
606 Straube, A., Hause, G., Fink, G., & Steinberg, G. (2006). Conventional kinesin mediates
607 microtubule-microtubule interactions in vivo. *Mol Biol Cell, 17*(2), 907-916. Retrieved
608 from https://www.ncbi.nlm.nih.gov/pubmed/16339079. doi:10.1091/mbc.e05-06-0542
609 Tabei, S. M. A., Burov, S., Kim, H. Y., Kuznetsov, A., Huynh, T., Jureller, J., . . . Scherer, N. F.
610 (2013). Intracellular transport of insulin granules is a subordinated random walk.
611 *Proceedings of the National Academy of Sciences of the United States of America,*
612 *110*(13), 4911-4916. Retrieved from <Go to ISI>://WOS:000318031900023.
613 doi:10.1073/pnas.1221962110
614 Tanenbaum, M. E., Gilbert, L. A., Qi, L. S., Weissman, J. S., & Vale, R. D. (2014). A protein-tagging
615 system for signal amplification in gene expression and fluorescence imaging. *Cell,*
616 *159*(3), 635-646. Retrieved from https://www.ncbi.nlm.nih.gov/pubmed/25307933.
617 doi:10.1016/j.cell.2014.09.039
618 Trogden, K. P., Zhu, X., Lee, J. S., Wright, C. V. E., Gu, G., & Kaverina, I. (2019). Regulation of
619 Glucose-Dependent Golgi-Derived Microtubules by cAMP/EPAC2 Promotes Secretory
620 Vesicle Biogenesis in Pancreatic beta Cells. *Curr Biol, 29*(14), 2339-2350 e2335.
621 Retrieved from https://www.ncbi.nlm.nih.gov/pubmed/31303487.
622 doi:10.1016/j.cub.2019.06.032
623 Varadi, A., Ainscow, E. K., Allan, V. J., & Rutter, G. A. (2002). Involvement of conventional
624 kinesin in glucose-stimulated secretory granule movements and exocytosis in clonal
625 pancreatic beta-cells. *J Cell Sci, 115*(Pt 21), 4177-4189. Retrieved from
626 https://www.ncbi.nlm.nih.gov/pubmed/12356920

627 https://jcs.biologists.org/content/joces/115/21/4177.full.pdf. doi:10.1242/jcs.00083
628 Varadi, A., Tsuboi, T., Johnson-Cadwell, L. I., Allan, V. J., & Rutter, G. A. (2003). Kinesin I and
629 cytoplasmic dynein orchestrate glucose-stimulated insulin-containing vesicle
630 movements in clonal MIN6 beta-cells. *Biochem Biophys Res Commun, 311*(2), 272-282.
631 Retrieved from https://www.ncbi.nlm.nih.gov/pubmed/14592410.
632 doi:10.1016/j.bbrc.2003.09.208
633 Vukusic, K., Ponjavic, I., Buda, R., Risteski, P., & Tolic, I. M. (2021). Microtubule-sliding modules
634 based on kinesins EG5 and PRC1-dependent KIF4A drive human spindle elongation. *Dev*
635 *Cell, 56*(9), 1253-1267 e1210. Retrieved from
636 https://www.ncbi.nlm.nih.gov/pubmed/33910056. doi:10.1016/j.devcel.2021.04.005
637 Yu, I., Garnham, C. P., & Roll-Mecak, A. (2015). Writing and Reading the Tubulin Code. *J Biol*
638 *Chem, 290*(28), 17163-17172. Retrieved from
639 https://www.ncbi.nlm.nih.gov/pubmed/25957412. doi:10.1074/jbc.R115.637447
640 Zhu, X., Hu, R., Brissova, M., Stein, R. W., Powers, A. C., Gu, G., & Kaverina, I. (2015).
641 Microtubules Negatively Regulate Insulin Secretion in Pancreatic beta Cells. *Dev Cell,*
642 *34*(6), 656-668. Retrieved from https://www.ncbi.nlm.nih.gov/pubmed/26418295.
643 doi:10.1016/j.devcel.2015.08.020

644

Figures

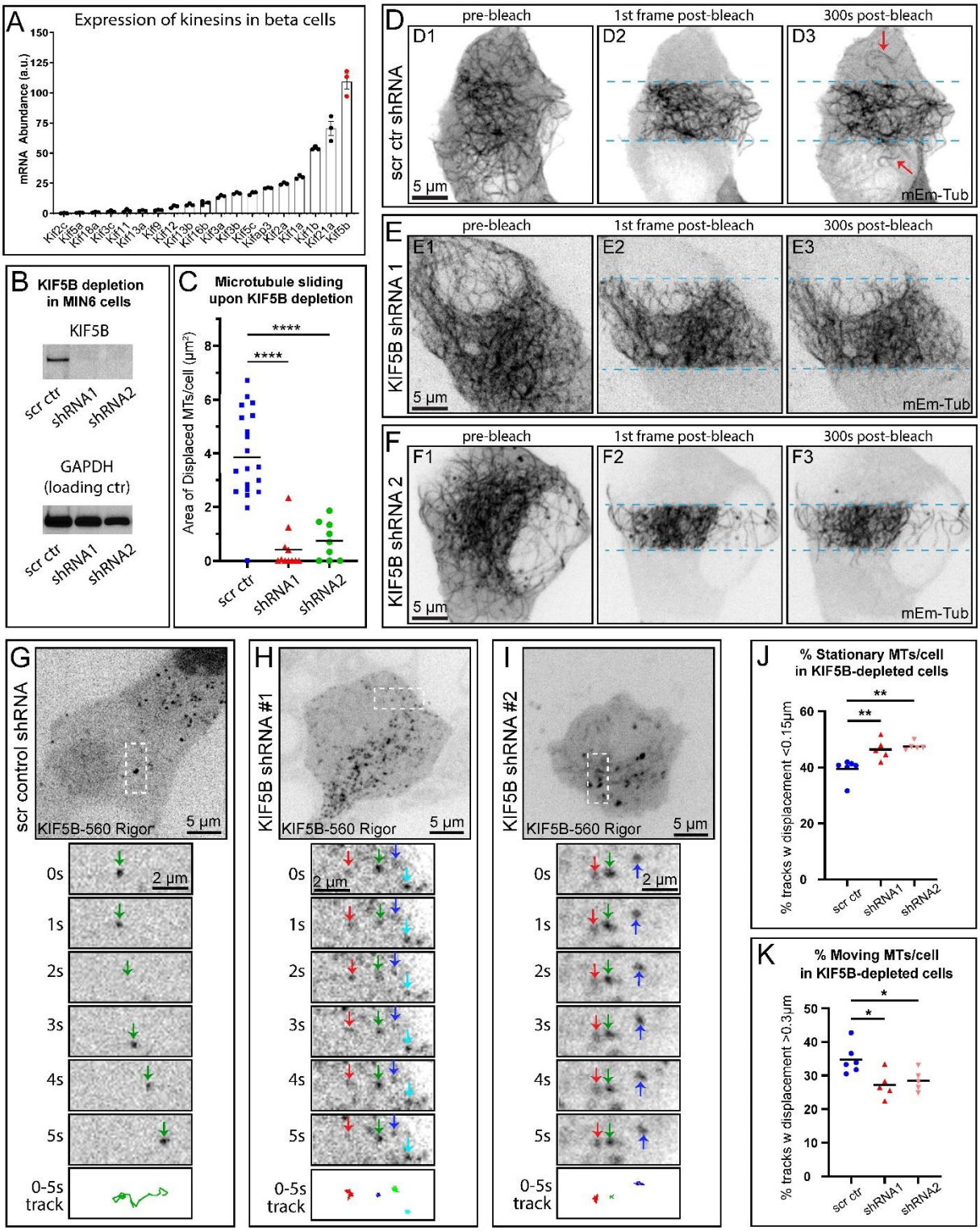
A
Expression of kinesins in beta cells
mRNA Abundance (a.u.)
Kif2c
Kif5a
Kif18a
Kif3c
Kif11
Kif13a
Kif9
Kif12
Kif13b
Kif16b
Kif20a
Kif3b
Kif5c
Kifap3
Kif2a
Kif1a
Kif1b
Kif21a
Kif5b
B
KIF5B depletion in MIN6 cells
KIF5B
scr ctr
shRNA1
shRNA2
GAPDH (loading ctr)
C
Microtubule sliding upon KIF5B depletion
Area of Displaced MTs/cell (μm²)
****
****
D
pre-bleach
1st frame post-bleach
300s post-bleach
scr ctr shRNA
D1
D2
D3
5 μm
mEm-Tub
E
KIF5B shRNA 1
E1
E2
E3
F
KIF5B shRNA 2
F1
F2
F3
G
scr control shRNA
KIF5B-560 Rigor
5 μm
2 μm
0s
1s
2s
3s
4s
5s
0-5s track
H
KIF5B shRNA #1
I
KIF5B shRNA #2
J
% Stationary MTs/cell in KIF5B-depleted cells
% tracks w displacement <0.15μm
**
**
K
% Moving MTs/cell in KIF5B-depleted cells
% tracks w displacement >0.3μm
*
*

Figure 1. MTs in pancreatic beta cells undergo extensive sliding driven by kinesin KIF5B.

A subset of RNA-sequencing data from primary mouse beta cells showing highly expressed kinesins as indicated by mRNA counts. KIF5B (most-right bar, red data points) is the most abundant kinesin motor in this cell type. N=3. Note that this is a subset of the RNA sequencing sets published in (Sanavia et al., 2021). (**B**) Efficient depletion of KIF5B in MIN6 cells using two alternative shRNA sequences, as compared to a scrambled shRNA control. GAPDH, loading control. Relevant ROIs from a Western blotting is shown. A representative example out of 3 repeats. (**C**) Quantification of MT sliding FRAP assay in cells treated with scrambled control or one of the two KIF5B-specific shRNAs (see representative data in D-F). MT displacement is shown as area of MTs displaced into the bleached area after 5 minutes of recovery. One-way ANOVA test was performed for statistical significance (p-value <0.0001). N=9-20 cells per set. (**D-F**) Frames from representative FRAP live-cell imaging sequences. mEmerald-tubulin-expressing MIN6 cells. Inverted grayscale images of maximum intensity projections over 1 µm-thick stacks by spinning disk confocal microscopy. (D1-F1) The last frame prior to photobleaching. (D2-F2) The first frame after photobleaching. (D3-F3) A frame 5 minutes (300 seconds) after photobleaching. Light-blue dotted lines indicate the edges of the photobleached areas. Red arrows indicate MTs displaced into the bleached area. Scale bars, 5 µm. (**G-I**) MIN6 cells featuring fiducial marks at MTs due to co-expression of SunTag-KIF5B-560Rigor construct and Halo-SunTag ligand. Representative examples for scrambled control shRNA-treated cell (G), KIF5B shRNA #1-treated cell (H) and KIF5B shRNA #2-treated cell (I) are shown. Single-slice spinning disk confocal

microscopy. Halo-tag signal is shown as inverted gray-scale image. Top panels show cell overviews (scale bars 5µm). Below, boxed insets (scale bars 2 µm) are enlarged to show dynamics of fiducial marks (color arrows) at 1 second intervals (1-5 seconds). 0- to 5-second tracks of fiducial mark movement are shown in the bottom panel, each track color-coded corresponding to the arrows in the image sequences. (**J**) Summarized quantification of stationary fraction of fiducial marks along MT lattice. Scrambled shRNA control N=1,421 tracks across 6 cells, shRNA#1 N=852 tracks across 5 cells, shRNA#2 N=679 tracks across 5 cells. P One-way ANOVA, $p<0.001$ (**K**) Summarized quantification of motile fraction of fiducial marks along the MT lattice. Scrambled shRNA control N=2,066 tracks across 6 cells, shRNA#1 N=390 tracks across 5 cells, shRNA#2 N=307 tracks across 5 cells. P One-way ANOVA, $p<0.001$

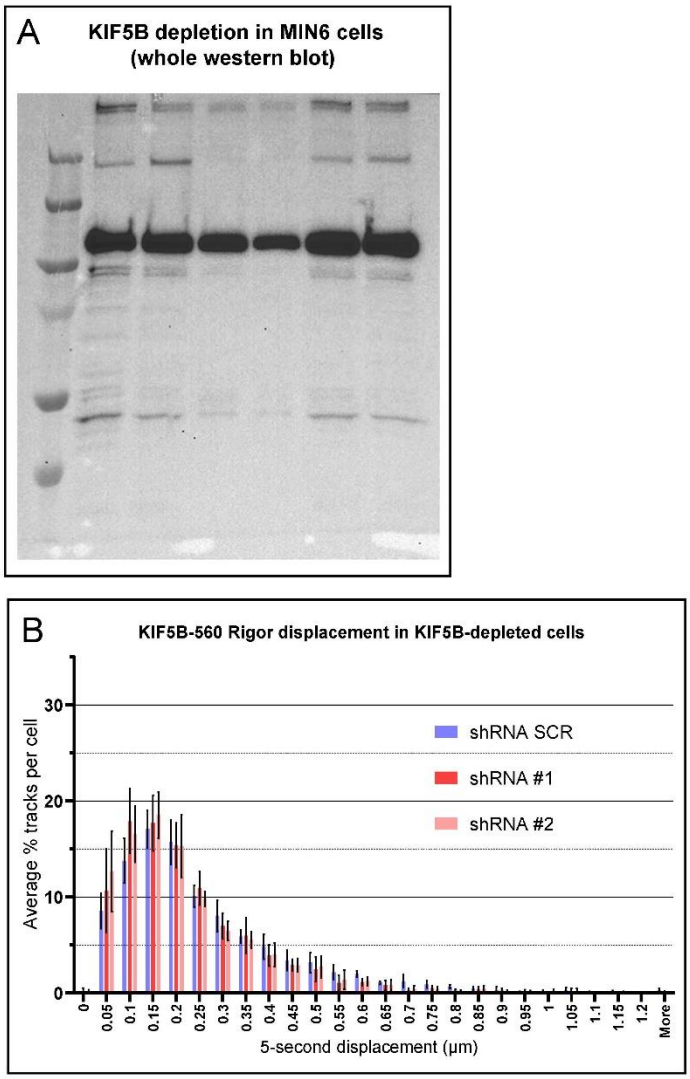

Figure 1 – Supplemental Figure 1.

(A) Full western blot of anti-kif5b from Fig. 1B. (**B**) Histogram of displacements over 5-second intervals for all fiducial marks in scrambled shRNA control vs KIF5B shRNA #1 and KIF5B shRNA #2.

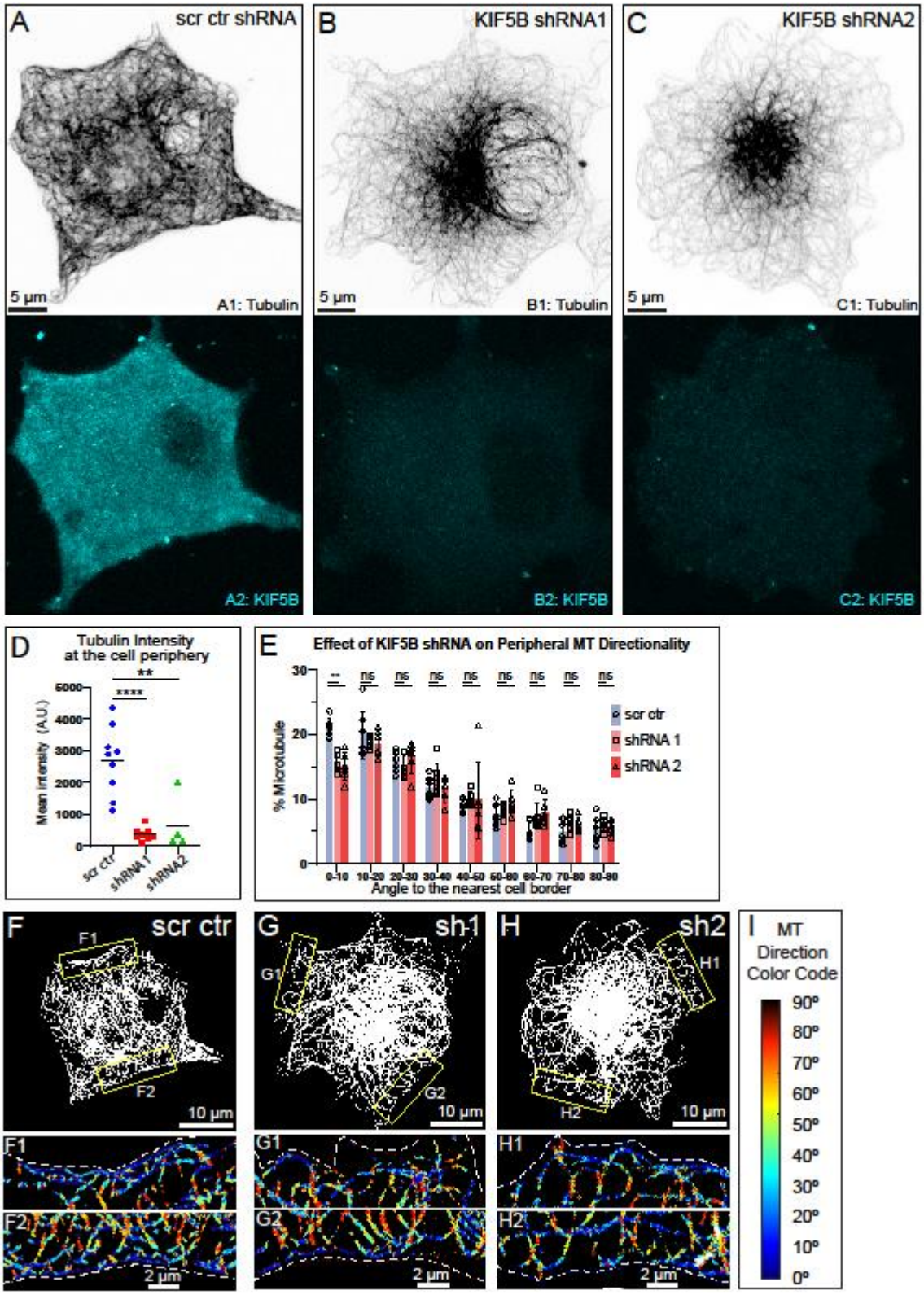

Figure 2. Microtubule abundance and alignment at the cell periphery depend on KIF5B.

(**A-C**) MT organization in MIN6 cells expressing scrambled control shRNA (A), KIF5B-targeting shRNA #1 (B), or KIF5B-targeting shRNA #2 (C). Top, immunofluorescence staining for tubulin (grayscale, inverted). Bottom, immunofluorescence staining for KIF5B (cyan). Laser scanning confocal microscopy maximum intensity projection of 1µm at the ventral side of the cell. N=12. Scale bars: 5um. (**D**) Quantification of mean tubulin intensity within the outer 2µm peripheral area of a cell, in data represented in (A-C). Mean values, black bars. One-way ANOVA, $p<0.0001$. N=5-9 cells. (**E**) Histograms of MT directionality within 1um of cell boundary using perfected thresholds (see Supplemental figure 2-1 for the analysis workflow) in cells treated with scrambled control versus KIF5B-targeting shRNA. Data are shown for the summarized detectable tubulin-positive pixels in the analyzed shRNA-treated cell population, as represented in (F-H). Unpaired t-test were performed across each bin for all cells, and a K-S test was performed on the overall distribution. The share of MTs parallel to the edge (bin 0-10) is significantly higher in control as compared to KIF5B depletions. Pixel numbers in the analysis: SCR N=106,741 pixels across 9 cells, shRNA #1 N=71,243 across 7 cells, shRNA #2 N= 54,101 across 7 cells. (**F-H**) Representative examples of MT directionality analysis quantified in (E). (**F**) Scrambled control shRNA-treated cell. (**G**) KIF5B shRNA #1-treated cell. (**H**) KIF5B shRNA#1-treated cell. Overviews of cellular MT networks are shown as threshold to detect individual peripheral MTs (see Supplemental figure 2-1 panel A5). (**F1-H2**) Directionality analysis outputs of regions from yellow boxes in (F-H) are shown color-coded for the angles between MTs and the nearest cell border. (**I**) Color code for (F1-H2): MTs parallel to the cell edge, blue; MTs perpendicular to the cell edge, red. Figure 2- Source Data 1

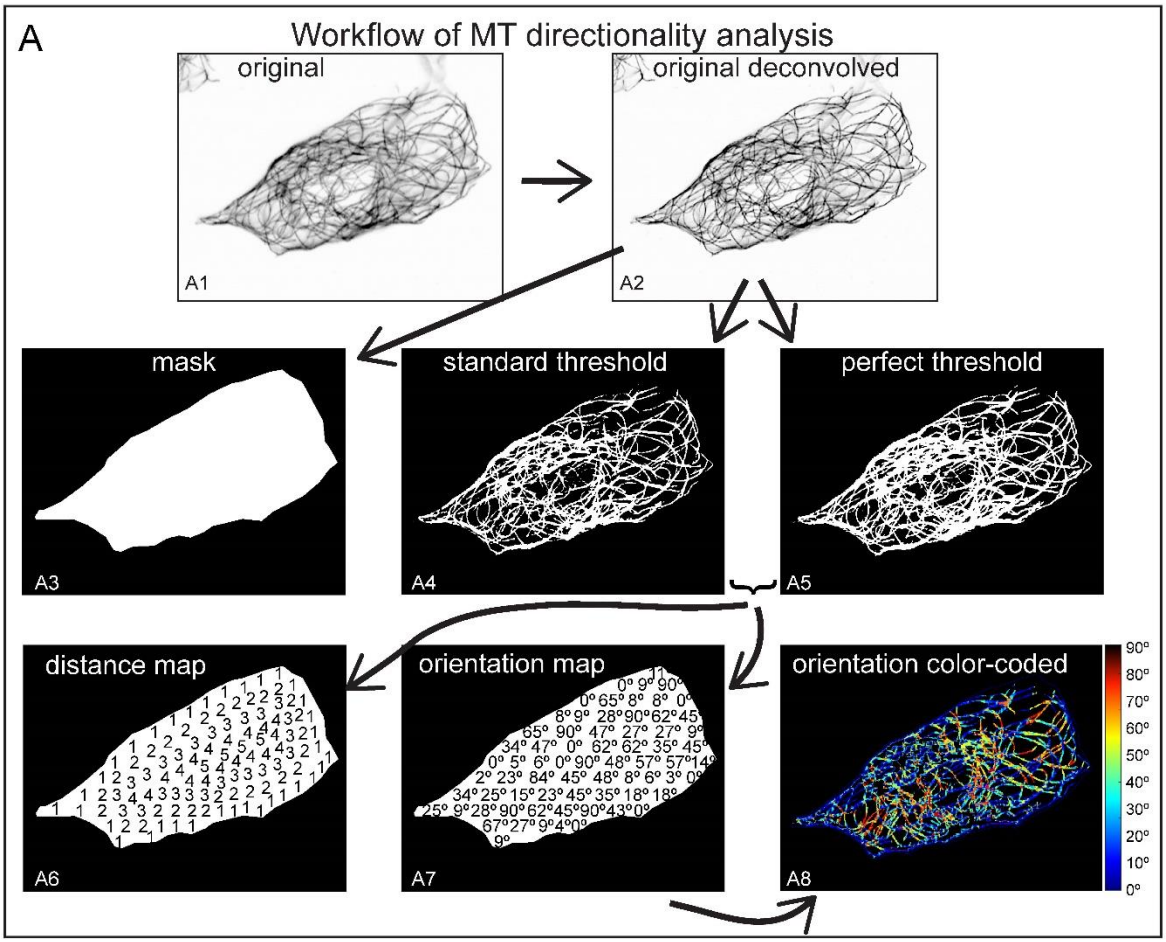

Figure 2 – Supplemental Figure 1. Workflow of MT directionality analysis.

(**A**) Representation of the analysis workflow using a control DMSO-treated cell immunostained for tubulin as an example. (A1) An image of the original inverted grayscale confocal slice. (A2) A deconvolved image. (A3) Mask of the cell boundary. (A4) An image within the mask after application of standard % threshold. (A5) An image within the mask after application of a threshold optimizing detection of peripheral MTs for a particular cell. (A3-A5) are derivatives of (A2). (A6) A schematic illustrating map of distances from the nearest cell (mask) border per pixel (not to scale). (A7) A schematic

illustrating map of angles per pixel (not to scale). A6 and A7 can be produced from A4 or A5. (A8) Color-coded output map of MT directionalities. A8 is a derivative of A7.

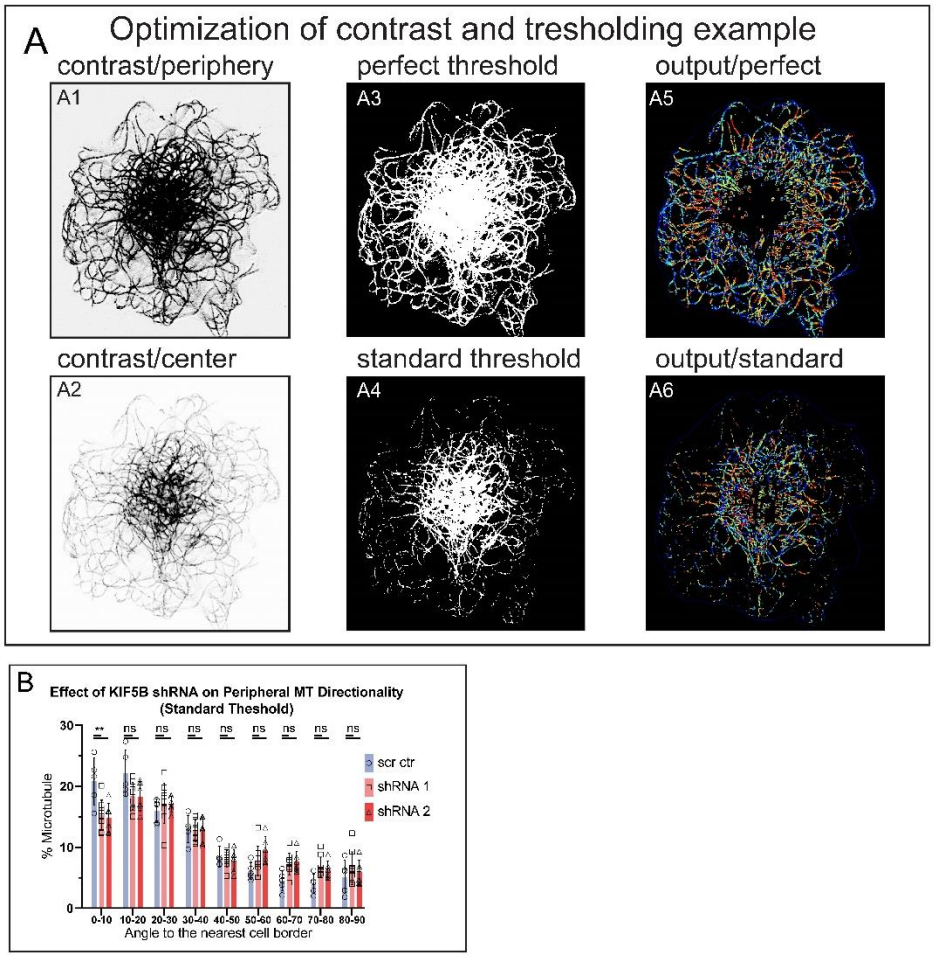

Figure 2-Supplemental Figure 2. Illustration of thresholding variations and their influence on the output analysis.

(**A**) A KIF5B-depleted cell as an example of contrast/threshold optimization for different MT densities and corresponding outputs. (A1) An deconvolved inverted grayscale confocal slice image contrasted to highlight peripheral MTs. (A2) The same deconvolved inverted grayscale confocal slice image contrasted to highlight central MTs. (A3) The image from A1 after application of a threshold optimized to highlight peripheral MTs. (A4) The image from A1 after application of a standard % threshold.

(A5) Analysis outcome from (A3). (A6) Analysis outcome from (A4). (**B**) Histograms of MT directionality within 1um of cell boundary using standard thresholds (see Supplemental figure 3/1 for the analysis workflow) in cells treated with scrambled control versus KIF5B-targeting shRNA. Data are shown for the summarized detectable tubulin-positive pixels in the analyzed shRNA-treated cell population, as represented in (F-H). Unpaired t-test were performed across each bin for all cells, and a K-S test was performed on the overall distribution. The share of MTs parallel to the edge (bin 0-10) is significantly higher in control as compared to KIF5B depletions. Pixel numbers in the analysis: SCR N=61,437 pixels across 9 cells, shRNA#1 N=15,215 pixels across 7 cells, shRNA#2 N= 21,125 pixels across 7 cells.

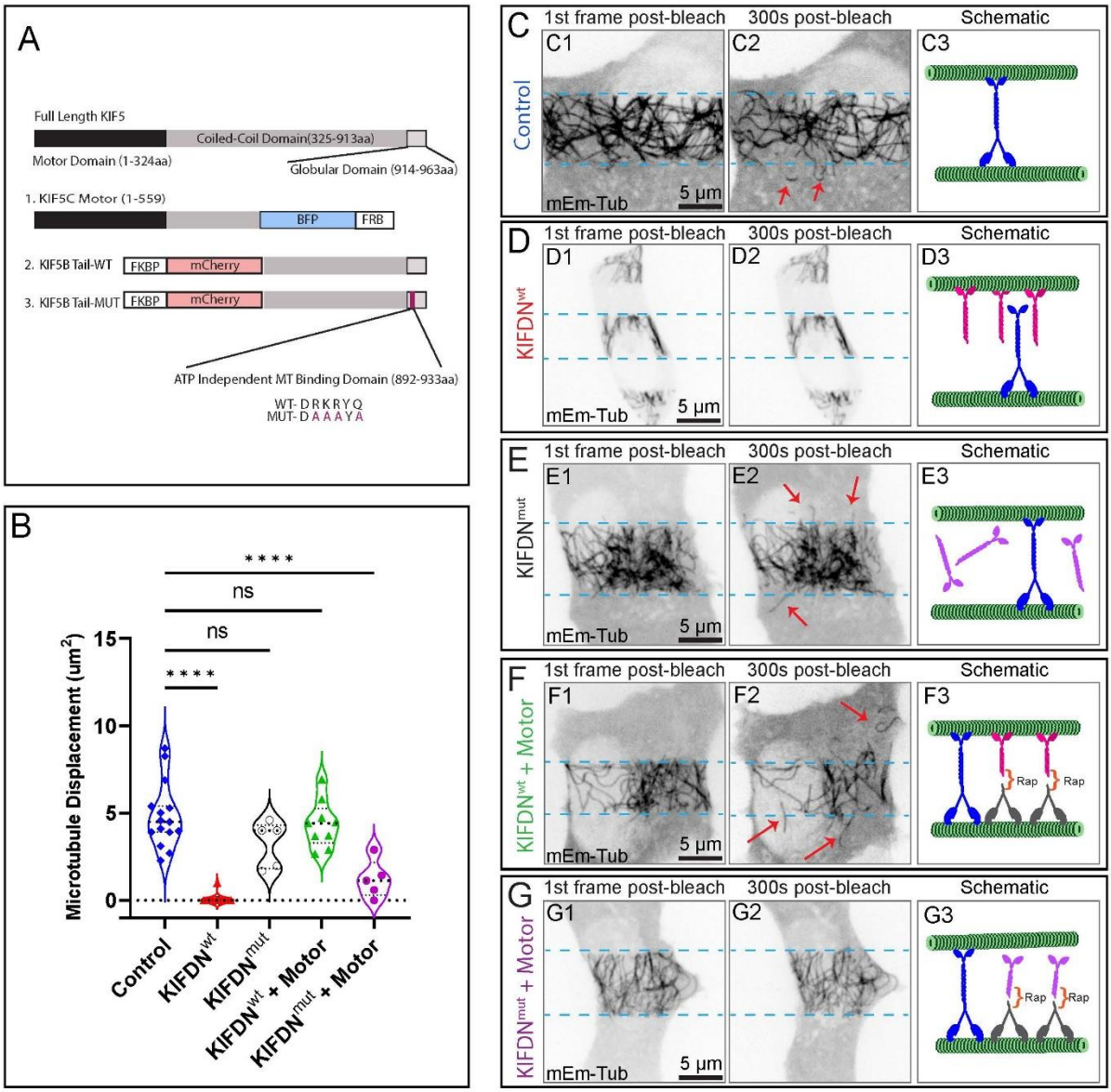

Figure 3. Microtubule sliding is facilitated through the ATP-independent MT-binding domain of kinesin-1.

(**A**) Schematic of kinesin-1 (KIF5) and the Dominant Negative (KIFDN) and heterodimerization strategy. Top schematic shows full length KIF5s, consisting of the motor domain, stalk coil-coil domain and the tail. Three constructs utilized here include (1) The KIF5C motor domain tagged with a blue fluorescent protein (BFP) and the FRB

for heterodimerization; (2) KIFDN^{wt} construct with KIF5B Tail domain tagged with the mCherry fluorescent protein and the FKBP for heterodimerization. (3) KIFDN^{mut} construct is the same as (2) but features a set of point mutations (magenta) making the ATP-independent MT-binding domain unable to bind MT lattice. (**B**) Quantification of MT sliding in FRAP assay in cells subjected to DN construct expression and heterodimerization (shown as area of displaced MTs). MT displacement is shown as area of MTs displaced into the bleached area after 5 minutes of recovery. See representative data (**C-G**). N= 5-25 per condition. One-way ANOVA test was performed for statistical significance (p-value <0.0001; ns, non-significant). **(C-G")** Frames from representative FRAP live-cell imaging sequences. mEmerald-tubulin-expressing MIN6 cells. Inverted grayscale images of maximum intensity projections over 1 µm-thick stacks by spinning disk confocal microscopy. (C1-G1) The first frame after photobleaching. (C2-G2) A frame 5 minutes (300 seconds) after photobleaching. Light-blue dotted lines indicate the edges of the photobleached areas. Red arrows indicate MTs displaced into the bleached area. Scale bars, 5 µm. (C3-G3) Schematics of experimental manipulation: green represents MTs, blue represents endogenous KIF5B, magenta represents KIFDN^{wt}, purple represents KIFDN^{mut}, gray represents KIF5C motor, orange bracket represents heterodimerizing agent (rap, rapalog). Conditions: (**C1-C3**) Untreated control. Only endogenous KIF5B is present. (**D1-D3**) KIFDN^{wt} overexpression. Endogenous KIF5B is unable to bind MTs. (**E1-E3**) KIFDN^{mut} overexpression. It does not bind MTs and does not interfere with endogenous KIF5B. (**F1-F3**) KIFDN^{wt} and KIF5C motor overexpression plus rapalog treatment. Heterodimerization creates a large pool of motors capable of MT sliding. (**G-**

G”) KIFDN^{mut} and KIF5C motor overexpression plus rapalog treatment. Heterodimerization creates a large pool of the motor non-functional in MT sliding.

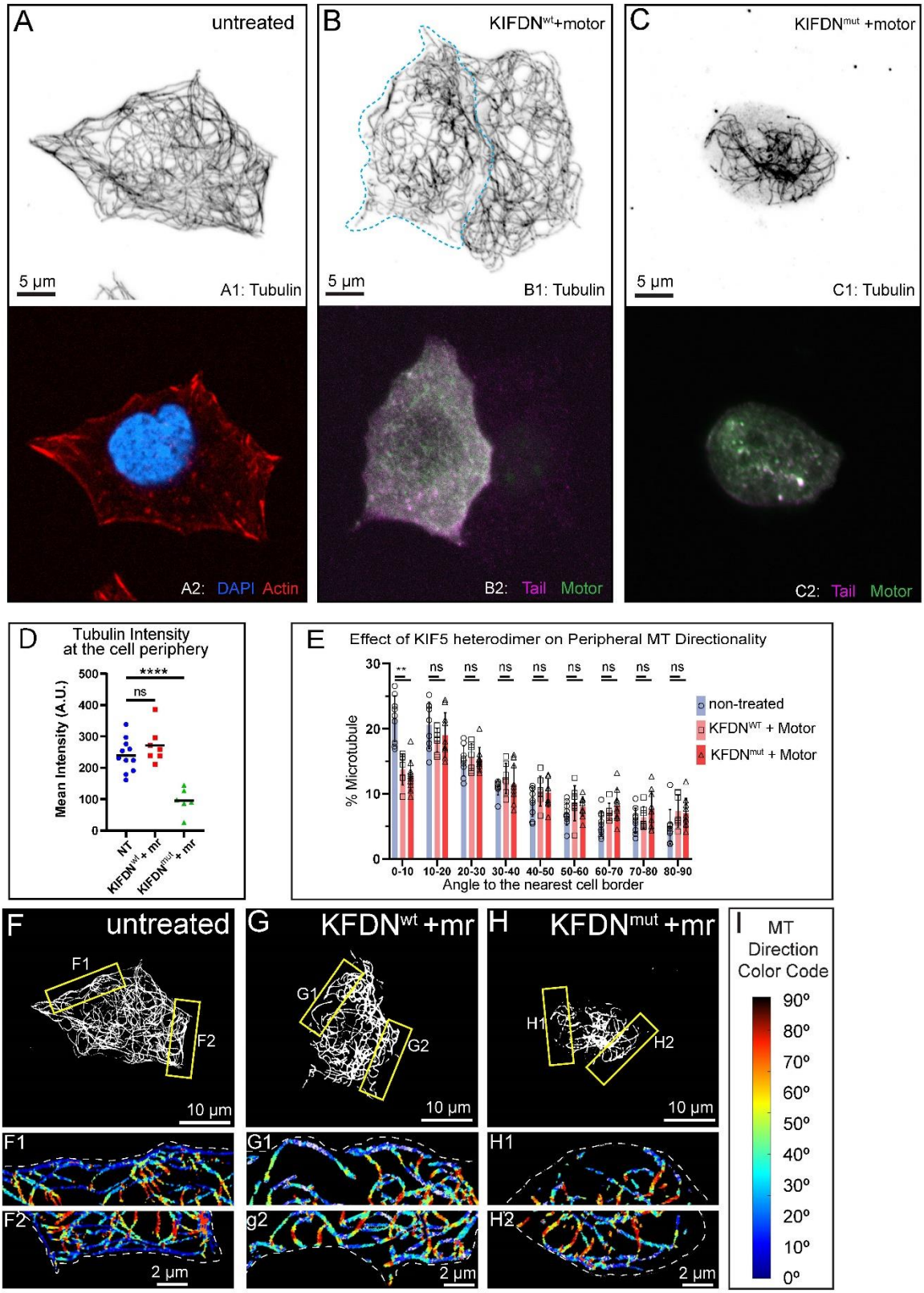
A
untreated
5 µm
A1: Tubulin
A2: DAPI Actin
B
KIFDNwt+motor
5 µm
B1: Tubulin
B2: Tail Motor
C
KIFDNmut +motor
5 µm
C1: Tubulin
C2: Tail Motor
D
Tubulin Intensity
at the cell periphery
Mean Intensity (A.U.)
500
400
300
200
100
0
****
ns
NT
KIFDNwt + mr
KIFDNmut + mr
E
Effect of KIF5 heterodimer on Peripheral MT Directionality
% Microtubule
30
20
10
0
**
ns
non-treated
KFDNWT + Motor
KFDNmut + Motor
0-10
10-20
20-30
30-40
40-50
50-60
60-70
70-80
80-90
Angle to the nearest cell border
F
untreated
F1
F2
10 µm
G
KFDNwt +mr
G1
G2
10 µm
H
KFDNmut +mr
H1
H2
10 µm
F1
F2
2 µm
G1
g2
2 µm
H1
H2
2 µm
I
MT
Direction
Color Code
90º
80º
70º
60º
50º
40º
30º
20º
10º
0º

786

Figure 4. Effects of ATP-independent MT-binding domain of KIF5B on microtubule abundance and alignment at the beta-cell cell periphery.

(**A-C**) MT organization in MIN6 cells expressing (**B**) KIFDN^{wt} and KIF5C motor heterodimerized via rapalog treatment, (**C**) KIFDN^{mut} and KIF5C motor heterodimerized via rapalog treatment and compared to a control cell with no ectopic expressions (**A**). Top, immunofluorescence staining for tubulin (grayscale, inverted). Blue dotted line indicates the borders of a cell expressing constructs of interest. Bottom in A, f-actin (phalloidin, red) and DAPI (blue). Bottom in B and C, ectopically expressed mCherry-labeled KIFDN constructs (magenta) and BFP-labeled KIF5C motor (green). Laser scanning confocal microscopy maximum intensity projection of 1µm at the ventral side of the cell. Scale bars: 5um. (**D**) Quantification of mean tubulin intensity within the outer 2µm peripheral area of a cell, in data represented in (A-C). Mean values, black bars. One-way ANOVA, $p<0.0001$. N=5-15 cells. (**E**) Histograms of MT directionality within 1um of cell boundary (see Supplemental figure 2-1 for the analysis workflow) in control cells compared to cells expressing heterodimerized KIFDN variants. Data are shown for the summarized detectable tubulin-positive pixels in the analyzed cell population, as represented in (F-H). Unpaired t-test were performed across each bin for all cells, and a K-S test was performed on the overall distribution. The share of MTs parallel to the edge (bin 0-10) is significantly higher in control as compared to the over-expressions. NT control N=138,810 pixels across 9 cells, KIFDN^{wt} + motor N= 48,285 pixels across 9 cells, KIFDN^{mut} + motor N= 40,832 pixels across 10 cells. (**F-H**) Representative examples of MT directionality analysis quantified in (E). (**F**) Control cell, no ectopic expressions. (**G**) Cell expressing KIFDN^{wt}+ Motor. (**H**) Cell expressing KIFDN^{mut}+ Motor.

Overviews of cellular MT networks are shown as threshold to detect individual peripheral MTs (see Supplemental figure 2-1 panel A5). (**F1-H2**) Directionality analysis outputs of regions from yellow boxes in (F-H) are shown color-coded for the angles between MTs and the nearest cell border (see Supplemental figure 2-1 panel A8). (**I**) Color code for (F1-H2): MTs parallel to the cell edge, blue; MTs perpendicular to the cell edge, red. Figure 4- Source Data 1

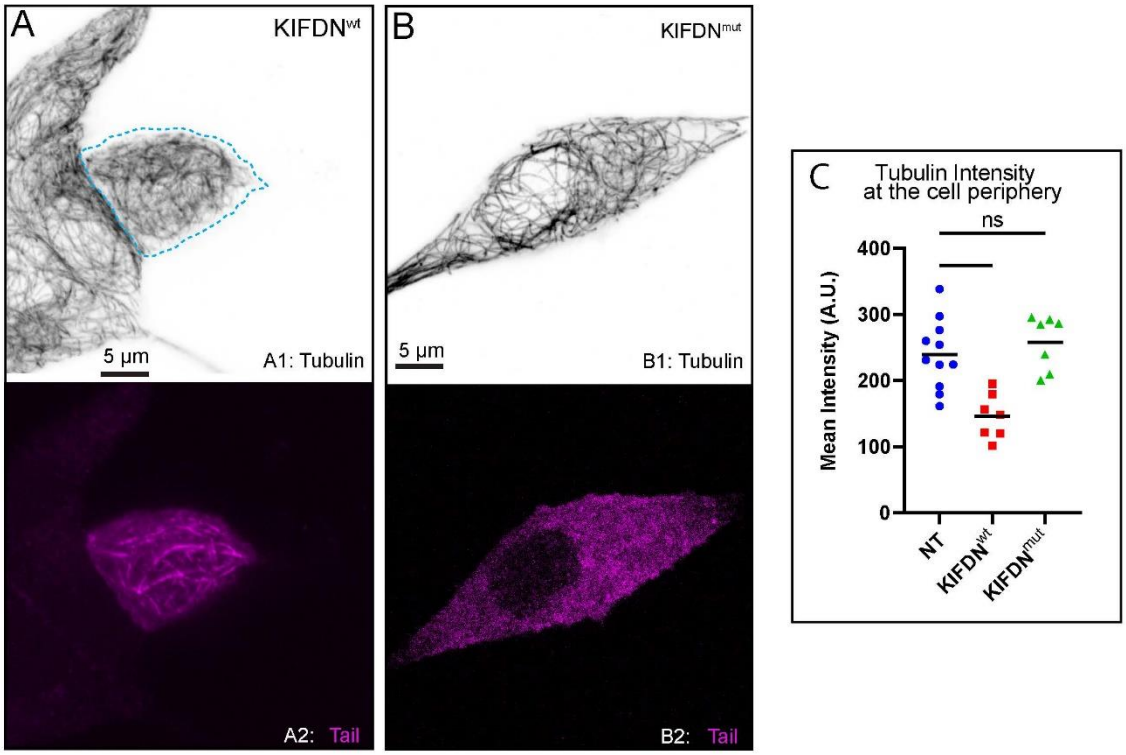

Figure 4 - Supplemental Figure 1. DN effect of KIF5B tail domain on MT abundance at the beta-cell cell periphery requires ATP-independent MT-binding domain. (**A-B**) MT organization in MIN6 cells expressing (**A**) KIFDN^{wt}, (**B**) KIFDN^{mut}, Top, immunofluorescence staining for tubulin (grayscale, inverted). Blue dotted line indicates the borders of a cell expressing constructs of interest. Bottom, ectopically expressed mCherry-labeled KIFDN constructs (magenta). Laser scanning confocal microscopy maximum intensity projection of 1µm at the ventral side of the cell. Scale bars: 5um. (**E**) Quantification of mean tubulin intensity within the outer 2µm peripheral area of a cell, in data represented in (A-B) as compared to untreated controls (see Figure 4A). Mean values, black bars. One-way ANOVA, $p<0.0001$. N=7-11 cells.

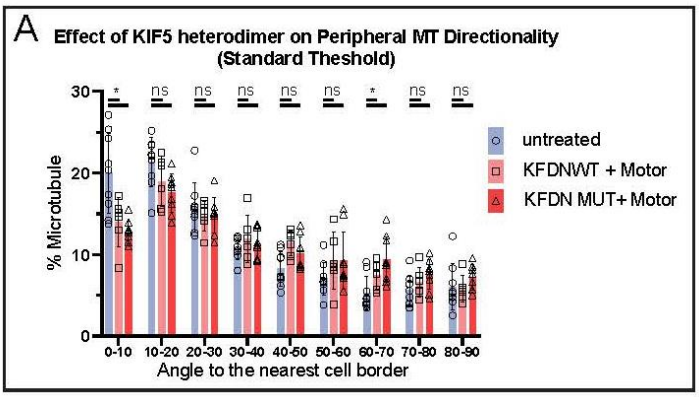

Figure 4-Supplemental Figure 2. Influence of thresholding variations on the output analysis of MT directionality in Figure 4 F-H. (**A**) Histograms of MT directionality within 1um of cell boundary using standard thresholds (see Supplemental figure 2-1 for the analysis workflow) in cells expressing ectopic heterodimerized KIF5C motor. Data are shown for the summarized detectable tubulin-positive pixels in the analyzed shRNA-treated cell population, as represented in (Figure 4 F-H). Unpaired t-test were performed across each bin for all cells, and a K-S test was performed on the overall distribution. The share of MTs parallel to the edge (bin 0-10) is significantly higher in control as compared to heterodimerized KIF5B over-expression. Pixel numbers in the analysis: NT control N=120,959 pixels across 9 cells, KIFDN^{wt} + motor N= 26, 110 pixels across 7 cells, KIFDN^{mut} + motor N= 41,091 pixels across 10 cells.

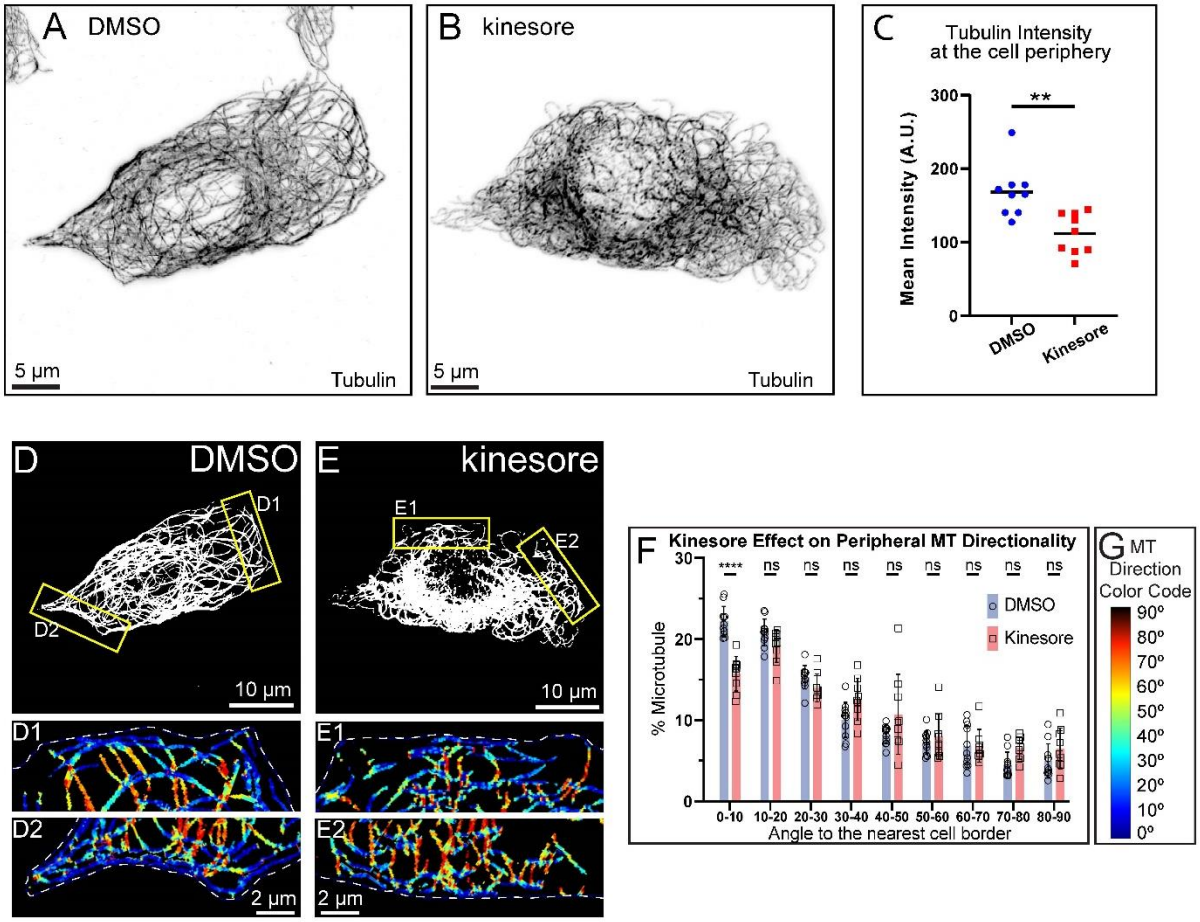

Figure 5 Enhanced MT sliding results in loss of peripheral MT alignment at the border

(A-B) MT organization in MIN6 cells pretreated with DMSO and Kinesore respectively. Immunofluorescence staining for tubulin (grayscale, inverted). Laser scanning confocal microscopy maximum intensity projection of 1µm at the ventral side of the cell. Scale bars: 5um. (**C**) Quantification of mean tubulin intensity within the outer 2µm peripheral area of a cell, in data represented in (A-B). Mean values, black bars. One-way ANOVA, $p<0.0001$. N=10 cells per condition. Histograms of MT directionality within 1um of cell boundary (see Supplemental figure 2-1 for the analysis workflow) in DMSO treated control cells compared to kinesore treated cells. Data are shown for the summarized

detectable tubulin-positive pixels in the analyzed cell population, as represented in (D-E). Unpaired t-test were performed across each bin for all cells, and a K-S test was performed on the overall distribution. The share of MTs parallel to the edge (bin 0-10) is significantly higher in control as compared to the over-expressions. DMSO control N=136,840 pixels across 10 cells, kinesore treated N= 87,361 pixels across 9 cells. (**D-E**) Representative examples of MT directionality analysis quantified in (F). Directionality analysis outputs of regions from yellow boxes in (D-E) are shown color-coded for the angles between MTs and the nearest cell border (see Supplemental figure 2-1 panel A8). (G) Color code for (D1-E2): MTs parallel to the cell edge, blue; MTs perpendicular to the cell edge, red. Figure 5- Source Data 1

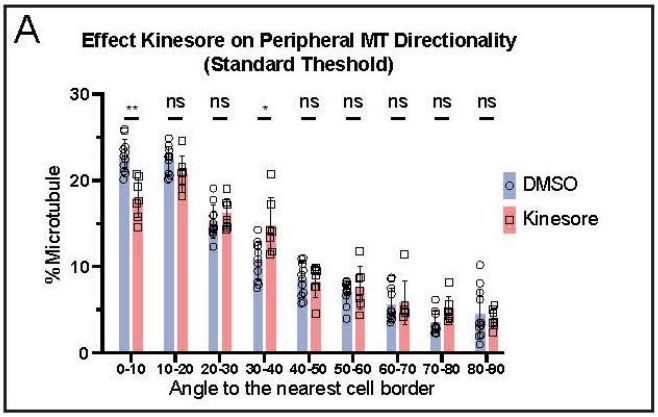

Figure 5-Supplemental Figure 1. Influence of thresholding variations on the output analysis of MT directionality in Figure 5 D-E. (**A**) Histograms of MT directionality within 1um of cell boundary using standard thresholds (see Supplemental figure 2-1 for the analysis workflow) in cells treated with DMSO or kinesore. Data are shown for the summarized detectable tubulin-positive pixels in the analyzed respective cell population, as represented in (Figure 5 D-E). Unpaired t-test were performed across each bin for all cells, and a K-S test was performed on the overall distribution. The share of MTs parallel to the edge (bin 0-10) is significantly higher in control as compared to kinesore treated. Pixel numbers in the analysis: DMSO control N= 94,841pixels across 9 cells, kinesore N= 29,796 pixels across 9 cells.

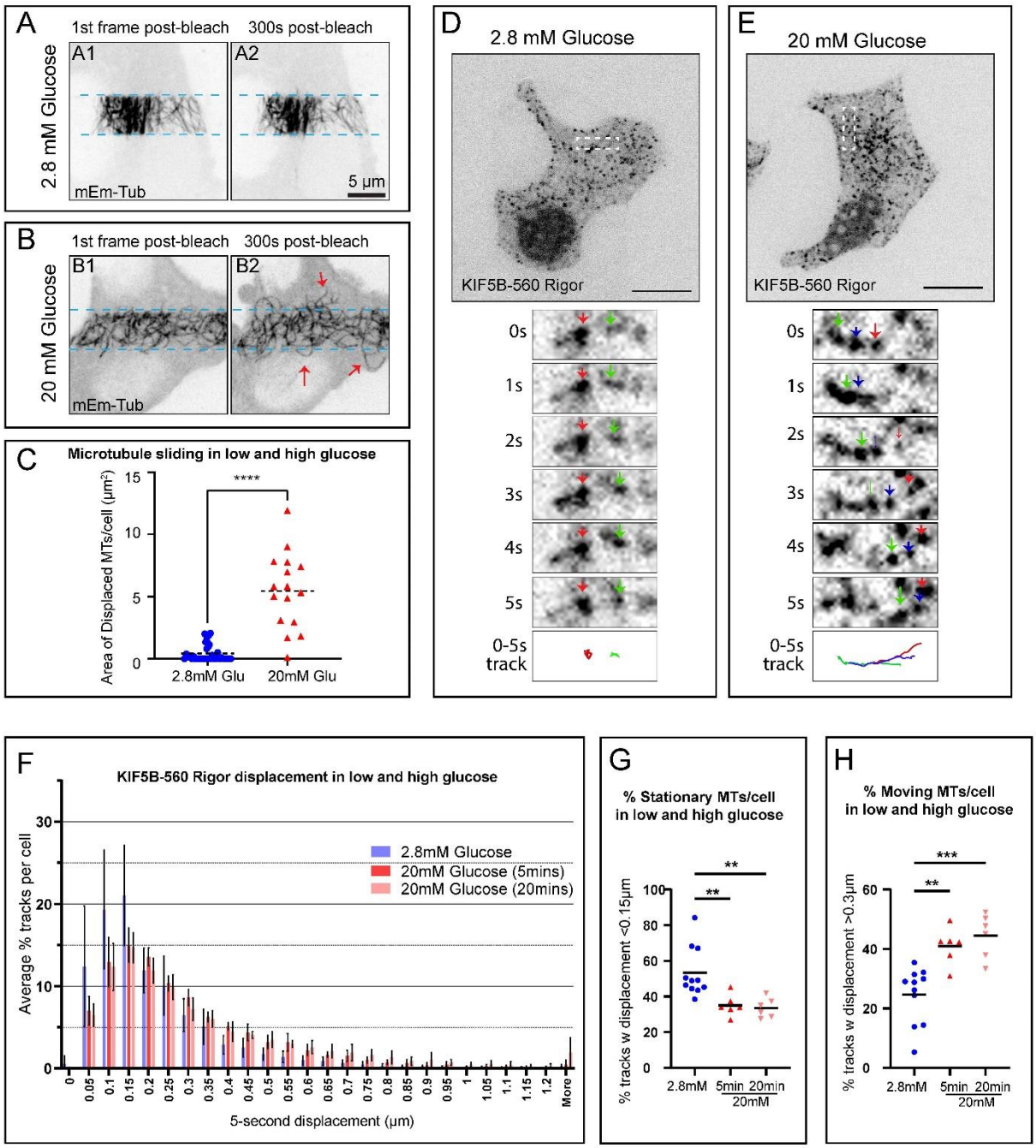

Figure 6. MT sliding in beta cells is stimulated by glucose.

(**A-B**) Frames from representative FRAP live-cell imaging sequences of MT sliding response to glucose stimulation. mEmerald-tubulin-expressing MIN6 cells. Inverted grayscale images of maximum intensity projections over 1 µm-thick stacks by spinning

disk confocal microscopy. (**A**) A cell pretreated with 2.8mM glucose before the assay. (**B**) A cell pretreated with 2.8mM glucose and stimulated with 20 mM glucose before the assay. (**A1-B1**) The first frame after photobleaching. (**A2-B2**) A frame 5 minutes (300 seconds) after photobleaching. Light-blue dotted lines indicate the edges of the photobleached areas. Red arrows indicate MTs displaced into the bleached area. Scale bars, 5 µm. (**C**) Quantification of MT sliding FRAP assay in cells in 2.8mM versus 20mM glucose (see representative data in A-B). MT displacement is shown as area of MTs displaced into the bleached area after 5 minutes of recovery. One-way ANOVA test was performed for statistical significance (p-value <0.0001). N=16-24 cells per set. (**D-E**) MIN6 cells featuring fiducial marks at MTs due to co-expression of SunTag-KIF5B-560Rigor construct and Halo-SunTag ligand. Representative examples for cells in 2.8mM glucose (D) and a cell stimulated by 20mM glucose (E) are shown. Single-slice spinning disk confocal microscopy. Halo-tag signal is shown as inverted gray-scale image. Top panels show cell overviews (scale bars 5µm). Below, boxed insets are enlarged to show dynamics of fiducial marks (color arrows) at 1 second intervals (1-5 seconds). 0- to 5-second tracks of fiducial mark movement are shown in the bottom panel, each track color-coded corresponding to the arrows in the image sequences. N=6-11 cells. (**F**) Histogram of all 5- second displacement of fiducial marks in Low vs High glucose (**G**) Summarized quantification of stationary fiducial marks along MT lattice. Low glucose N=5,615 tracks across 11 cells, High glucose 5min N=2,259 tracks across 6 cells, High Glucose 20min N=3,059 tracks across 6 cells. P One-way ANOVA, p<0.001 (**H**) Summarized quantification of moving fiducial marks along the MT lattice.

Low glucose N=2,595 tracks across 11 cells, High glucose 5min N=2,642 tracks across 6 cells, High Glucose 20min N=4,049 tracks across 6 cells. One-way ANOVA, $p<0.001$.

Video Titles

Figure 1-Video 1

KIF5B-mediated MT sliding visualization via FRAP. Cells treated with scrambled control and two shRNAs against KIF5B are shown. Time, minutes:seconds.

Figure 1-Video 2

KIF5B-mediated MT sliding visualization via SunTag-KIF5B-560Rigor. Cells treated with scrambled control and two shRNAs against KIF5B are shown. Sliding maximum intensity projection (15 time frames projected in each video frame). Time, seconds.

Figure 3-Video 1

Dominant Negative MT sliding visualization via FRAP (Tails). Cells over-expressing $KIFDN^{wt}$ versus $KIFDN^{mut}$ are shown. Time, minutes:seconds.

Figure 3-Video 2

Dominant Negative MT sliding via FRAP (Tails + Motors). Cells expressing heterodimerized $KIFDN^{wt}$ with motor versus heterodimerized $KIFDN^{mut}$ with motor are shown. Time, minutes:seconds.

Figure 6-Video 1

Glucose-Dependent MT sliding visualization via FRAP. Cells in low versus high glucose are shown. Time, minutes:seconds

Figure 6-Video 2

Glucose-Dependent MT sliding visualization via SunTag-KIF5B-560Rigor. Cells in low versus high glucose are shown. Sliding maximum intensity projection (15 time frames projected in each video frame). Time, seconds.

Source Data

Figure 2- Source Data 1

MT Directionality Source Data: KIF5B Depletion

Figure 4- Source Data 1

MT Directionality Source Data: KIFDN Overexpression

Figure 5- Source Data 1

MT Directionality Source Data: Kinesore Treatment

Figure 6- Source Data 1

SunTag marks displacement 5s intervals across each cell. And population analysis referenced in panels G and H.